Department of Physics and Astronomy
University of Heidelberg

Bachelor Thesis in Physics
submitted by

Nadine Grünwald

born in Lindenfels (Germany)

2020

Simultaneous blast-wave description of transverse momentum spectra and elliptic flow data at $\sqrt{s_{\mathrm{NN}}} = 7.7$ GeV - 5.02 TeV

This Bachelor Thesis has been carried out by Nadine Grünwald at the
Physikalisches Institut in Heidelberg
under the supervision of
Prof. Dr. Johanna Stachel

Abstract

Simultaneous blast-wave fits to spectra and elliptic flow data measured at various beam energies are carried out in this bachelor thesis. Fits to $\sqrt{s_{\mathrm{NN}}} = 5.02$, 2.76 TeV and 200 GeV data, recorded in A-A collisions are done concerning the question if heavy quarks are thermalized in the QGP. The spectra and elliptic flow data of the Υ ($\mathrm{b\overline{b}}$), J/ψ ($\mathrm{c\overline{c}}$) and D^0 ($\mathrm{\overline{u}c}$) mesons are included due to their heavy quark content. Various collision centralities and systematic variations of the transverse momentum fit ranges and the particles, which are included to the fits, are studied. While for the elliptic flow data a reasonable agreement of the blast-wave model is found, the deviations for the spectra, in particular the D^0 and J/ψ spectra, are larger. Due to the observed deviations a total thermalization of charm quarks is unlikely at the moment but further studies are still needed.

A similar study was performed with blast-wave fits at energies from $\sqrt{s_{\mathrm{NN}}} = 7.7 - 62.4$ GeV taken during the Beam Energy Scan (BES) program at RHIC. For the first time particle and anti-particle spectra were included for simultaneous fits. This enables the extraction of the kinetic freeze-out temperature (T_{kin}). In addition the fit results for LHC energies are included and thus the behavior of T_{kin} and the mean flow velocity ($\langle\beta\rangle$) can be studied at the energy range of $\sqrt{s_{\mathrm{NN}}} = 7.7$ GeV - 5.02 TeV. At energies below 62.4 GeV a clear separation between the particle and anti-particle kinetic freeze-out temperature and mean flow velocity is observed which indicates that a global thermalization at low energies is unlikely.

In addition tools were developed to provide the data used for the analysis described above. About 1300 data sets were converted to make them usable for the blast-wave fit program. Those tools will be available for the community for easily importing and using the data for the blast-wave fits.

Zusammenfassung

In dieser Bachelorarbeit werden Transversalimpulsspektren und v_2 Daten für verschiedene Schwerpunktsenergien mit einem Blastwave Modell beschrieben. Um Hinweise auf eine mögliche Thermalisierung von schweren Quarks zu erhalten, werden Blastwave Fits an Daten, die in A-A Kollisionen bei $\sqrt{s_{\mathrm{NN}}} = 5.02$, 2.76 TeV und 200 GeV gemessen wurden, durchgeführt. Die Spektren und v_2 Daten der Υ ($\mathrm{b\overline{b}}$), J/ψ ($\mathrm{c\overline{c}}$) und D^0 ($\mathrm{\overline{u}c}$) Mesonen werden wegen ihrer schweren Quarks untersucht. Es werden verschiedene Zentralitäten verwendet und systematische Variationen der p_{T} Bereiche und der Teilchen, die für den Fit genutzt werden, durchgeführt. Es wird eine akzeptable Übereinstimmung des Blastwave Modells mit den v_2 Daten gefunden, jedoch beobachten wir Abweichungen des Blastwave Modells von den D^0 und J/ψ Spektren. Aufgrund der Abweichungen ist es unwahrscheinlich, dass Charm-Quarks an der globalen Thermalisierung beteiligt sind, jedoch sind weitere Untersuchungen notwendig.

Anschließend werden Blastwave Fits für Energien von $\sqrt{s_{\mathrm{NN}}} = 7.7 - 62.4$ GeV des Beam Energy Scan (BES) Programms durchgeführt. Erstmals können auch die Spektren von Teilchen und Antiteilchen für den Fit genutzt werden. Dadurch ist es möglich auch die Temperatur (T_{kin}) zu bestimmen, bei der die Teilchen thermisch ausfrieren. Dies ermöglicht außerdem die Untersuchung der Blastwave Parameter, T_{kin} und der mittleren Flussgeschwindigkeit ($\langle\beta\rangle$), bei allen Energien von $\sqrt{s_{\mathrm{NN}}} = 7.7$ GeV bis 5.02 TeV. Für Schwerpunktsenergien kleiner als 62.4 GeV werden klare Unterschiede zwischen Teilchen und Antiteilchen beobachtet, wodurch eine globale Thermalisierung unwahrscheinlich wird.

Zusätzlich wurde im Rahmen dieser Bachelorarbeit ein Programm entwickelt, welches für die Bereitstellung der Daten für die Analyse benötigt wurde. Mit diesem Programm wurden etwa 1300 Spektren und v_2 Daten umgewandelt, sodass diese im Hauptprogramm für die Blastwave Fits genutzt werden konnten, nachdem sie importiert wurden. Das Programm wird dem Nutzer zur Verfügung gestellt, um eine einfache Nutzung der Daten für die Blastwave Fits zu ermöglichen.

Contents

1 Introduction **1**
1.1 Heavy-ion collisions . . . 2
1.2 Blast-wave model . . . 4
1.3 Outline . . . 7

2 Data converting and importing tools **8**
2.1 Converting data . . . 8
2.2 Importing data to the main program . . . 13

3 Blast-wave fits to v_2 and dN/dp_T data measured in high energy collisions **15**
3.1 Fit results for $\sqrt{s_{NN}} = 2.76$ and 5.02 TeV . . . 15
3.2 Feed-down . . . 20
3.3 Systematic study of fits at $\sqrt{s_{NN}} = 200$ GeV . . . 21

4 Energy dependence of the blast-wave parameters and fits to $\sqrt{s_{NN}} = 7.7$-62.4 GeV **26**
4.1 Fit results for $\sqrt{s_{NN}} = 11.5$ and 39 GeV . . . 27
4.2 T_{kin} and $\langle\beta\rangle$ in dependence of the center-of-mass energy . . . 32

5 Summary and Outlook **36**

A Appendix **38**
A.1 Boost model . . . 38
A.2 Fit results for $\sqrt{s_{NN}} = 200$ GeV . . . 38
A.3 Fit parameters for $\sqrt{s_{NN}} = 7.7$ - 62.4 GeV . . . 40

Bibliography **41**

1 Introduction

A few microseconds after the big bang it is assumed that the universe was in a state of hot and dense matter with deconfined quarks and gluons [1]. This state is referred to as Quark Gluon Plasma (QGP). After the universe cooled down, the quarks and gluons are combined and the ordinary hadronic matter was built [2]. To learn more about this state of the early universe, the properties and the behavior of this strongly interacting many-body system under extreme conditions, the QGP is reproduced in the laboratory. This is realized in heavy ion collisions which are introduced in the next section. In heavy ion collisions it is possible to achieve the required temperature and density to create this new state of matter. While strong indications for the existence of the QGP were already found [3, 4], other questions about the properties and the behavior of the QGP are still open. Experiments at the Beam Energy Scan (BES) program at RHIC are carried out to get information about the phase transition from a hadron gas to QGP and in particular to locate the the critical point [5]. Other measurements are used to investigate transport properties of the QGP. The jet transport parameter is related to the energy loss of jets due to their strong interaction with the QGP [6]. The shear viscosity to entropy density ratio η/s is another quantity used to describe the hydrodynamical behavior of the QGP [7].

The field theory of the strong interaction is quantum chromodynamics (QCD), which is part of the Standard Model of particle physics. The Standard Model includes the electromagnetic, strong and weak interaction and all known fundamental particles, where fermions with half integer spin and bosons with integer spin are distinguished. The matter building particles, Leptons and Quarks, are fermions with spin 1/2. They are separated into three generations with increasing mass. The force carrying gauge-bosons are spin 1 particles and the Higgs boson, which is the reason for particles to have mass, if they are interacting with the Higgs field, has spin 0 [8, 9].

The strong interaction is mediated between quarks, listed in Tab. 1 , by one of the eight massless gluons. Quarks and gluons carry color charge. There are three colors (red, green, blue) and their corresponding anti-colors. All colored objects are confined into colorless hadronic states, which means quarks and gluons can not propagate as free particles and only exist in bound hadronic states. Only under extreme conditions, at high temperatures and/or densities, as achieved after the big bang or in heavy ion collisions, the quarks and gluons are deconfined.

The non relativistic QCD potential for a bound quark-antiquark pair is given by equation 1, where r is the distance between q and $\overline{\mathrm{q}}$, α_s is the strong coupling constant and κ~1GeV/fm [8].

$$V_{\mathrm{q}\overline{\mathrm{q}}}(r) = -\frac{4}{3}\frac{\alpha_\mathrm{s}}{r} + \kappa r \tag{1}$$

If one pulls apart a quark and anti-quark the energy gets high enough for building an additional $\mathrm{q}\overline{\mathrm{q}}$ pair. The coupling constant of the strong interaction α_s depends on the momentum transfer. With increasing momentum transfer, the coupling constant becomes smaller. At small distances and large momentum transfer quarks can be treated as asymptotically free particles [8].

Because the QGP is a strongly interacting many-body system of free quarks and gluons, dynamical calculations based on QCD are not possible with the exception of lattice QCD calculations. In order to derive information about this complex system, a combination of experimental measurements and descriptions by models are necessary. The blast-wave model is used to extract the kinetic freeze-out temperature and the flow velocity out of experimental data. In this bachelor thesis it is applied to spectra and elliptic flow data measured in Au-Au collisions at $\sqrt{s_\mathrm{NN}} = 7.7 - 200$ GeV and in Pb-Pb collisions at $\sqrt{s_\mathrm{NN}} = 2.76$ and 5.02 TeV. Simultaneous fits to spectra and elliptic flow data are carried out at 200 GeV to get indications about a possible thermalization of charm quarks in the QGP. In addition, fits to all energies are used to study the behavior of the kinetic freeze-out temperature and the mean flow velocity as a function of the energy.

Table 1: The different quark flavours, their corresponding charges and masses [10, 11]

	d	u	s	c	b	t
Charge (e)	-1/3	+2/3	-1/3	+2/3	-1/3	+2/3
Mass (GeV/c^2)	0.005	0.002	0.093	1.27	4.18	172.9

1.1 Heavy-ion collisions

Heavy-ions are collided at high energies to produce the QGP in the laboratory. Different ions and center-of-mass energies are used to investigate different areas in the QCD phase diagram of strongly interacting matter [12].

Between 1986 and 2003 at the CERN Super Proton Synchrotron (SPS) sulfur and later lead ions were collided with energies up to $\sqrt{s_{\mathrm{NN}}} = 20$ GeV. Starting in the same year and stopped in 2000, collisions with silicon/gold ions and $\sqrt{s_{\mathrm{NN}}} = 5$ GeV are observed at the AGS (Alternating Gradient Synchrotron) of the Brookhaven National Laboratory (BNL). Since 2000 heavy ion collisions of gold atoms with center-of-mass energies up to $\sqrt{s_{\mathrm{NN}}} = 200$ GeV are studied at the Relativistic Heavy Ion Collider (RHIC) at BNL. At the CERN LHC lead-lead collisions are performed since 2010. The two nuclei beams are accelerated up to an energy of $\sqrt{s_{\mathrm{NN}}}$= 5.5 TeV [13]. The commissioning of the FAIR (Facility for Antiproton and Ion Research) accelerator at GSI is planned for 2025. Ions of elements with atomic number 1-92 and anti-protons will be accelerated there [14].

Fig. 1 shows the space-time evolution of the QGP. After the collision at t = z = 0 and the pre-equilibrium time, the QGP is formed. The thermalized quarks can move freely and interact while the QGP expands and cools down. At a critical temperature the phase transition of the QGP to a hadron gas starts. After the chemical freeze-out temperature T_{ch} is reached, all quarks and anti-quarks are combined into colorless hadronic states and the energies of the hadrons become too low for inelastic collisions. The generated hadrons can interact elastically with each other until the temperature has fallen below the kinetic freeze-out temperature T_{kin}. Then the kinetic energies of the particles are fixed [15].

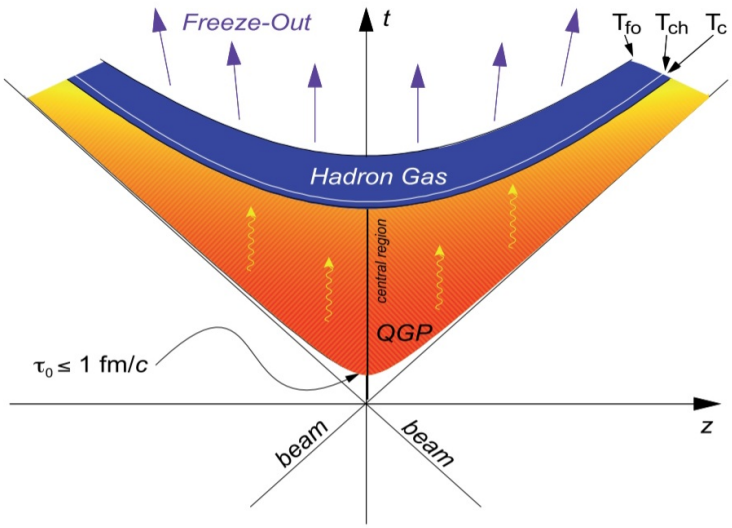

Figure 1: Space-time evolution of the QGP. At T_{c} the phase transition of the QGP to a hadron gas occurs. T_{ch} is the chemical freeze-out temperature at which all quarks and gluons are combined into hadrons. At T_{fo} (= T_{kin} kinetic freeze-out temperature) all particles momenta are fixed. Figure taken from [16].

Different experimental observables are used to derive information about the expansion and freeze-out of the QGP. Hadron yields (dN/dp_{T}) are measured for different particles as function of the transverse momentum $p_{\mathrm{T}} = \sqrt{p_{\mathrm{x}}^2 + p_{\mathrm{y}}^2}$ with the beam direction parallel to the z-axis. The centrality is

a measure of the geometrical overlap zone of the two colliding nuclei. A centrality of 0-5% corresponds to the most central collision with almost head on colliding ions.

The flow describes the collective behavior of the QGP. Due to the initial pressure the fireball expands in radial direction resulting in a radial flow component. Because the pressure and thus the radial flow is depending on the centrality of the collision one can see a centrality dependence of the transverse momentum spectra. The relative particle yields at higher p_{T} become larger for more central collisions due to this radial flow effect.

In addition an azimuthal anisotropy (transverse to the beam direction) in the transverse momentum spectra is observed for non central collisions. The upper part of Fig. 2 shows two colliding nuclei and their almond-shaped overlap region for a non central collision. This spatial anisotropy at the beginning of the collision leads to rescattering of the particles and results in a momentum anisotropy, shown in the lower part of Fig. 2. Because the pressure gradient is larger in x than in y-direction more particles are emitted in the reaction plane than out of this plane. The reaction plane is defined by the beam axis and the impact vector of the two colliding nuclei as depicted in Fig. 2. The anisotropy is described by the elliptic flow v_2, which reaches its maximum in the reaction plane and increases for more peripheral collisions [17, 18]. The elliptic flow v_2 is the second coefficient in the Fourier decomposition of the azimuthal particle distribution given in equation 2, where v_n are the Fourier coefficients and ϕ the azimuthal angle relative to the reaction plane [19].

$$\frac{dN}{d\phi} \propto 1 + 2\sum_{n=1} v_n(p_{\mathrm{T}}) cos(n\phi) \tag{2}$$

To connect the experimental measurements to transport properties, the evolution and freeze-out of the QGP different models are used. In the next section the hydrodynamic and in particular the blast-wave model are introduced.

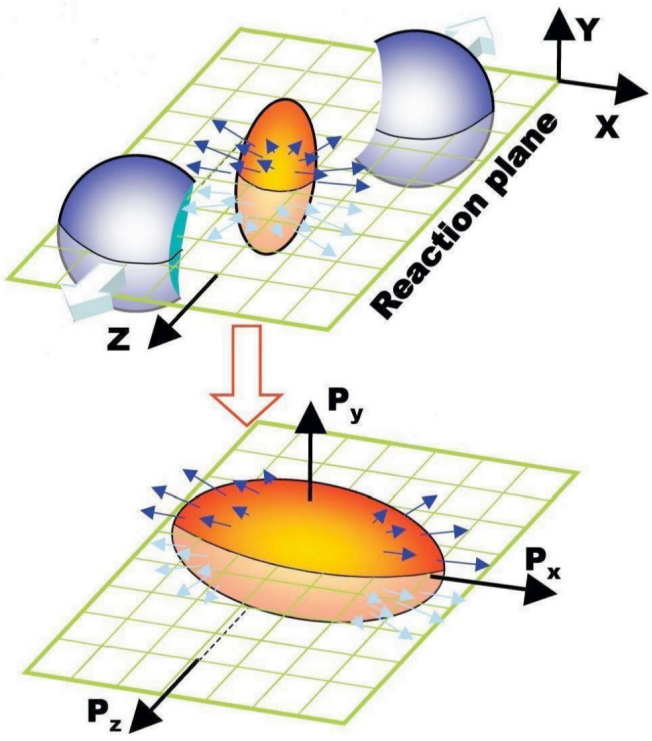

Figure 2: Upper: Non-central collision of two nuclei with spatial anisotropy. Lower: Resulting momentum anisotropy in the transverse x-y plane. Figure taken from [20]

1.2 Blast-wave model

The evolution of the QGP can be described by hydrodynamic models [7, 15]. To apply them it is assumed that the QGP is in local thermodynamic equilibrium. This is a necessary condition for a well defined temperature, density, entropy and pressure. Local thermal equilibrium is only reached if the free path length is small compared to the considered cell in the system. Additional conditions are necessary to describe the fluctuating initial state before the hydrodynamic evolution starts. A common model to derive them is the Glauber model [21]. Basically the evolution of the QGP is defined by the conservation laws and the equation of state. The agreement of ideal hydrodynamics with measured observables gave evidence for a strongly interacting system [7]. Better agreement with data is found by considering viscous hydrodynamics, including the shear viscosity to entropy density ratio η/s. The resulting particle spectra can be computed using the Cooper Frye formula, assuming a constant temperature or energy density at the freeze-out of the particles [7].

An alternative way to describe the behavior of the expansion and freeze-out of the QGP is provided by the blast-wave models. Based on the assumption that the QGP is fully thermalized and all particles freeze-out at the same temperature, they offer an easier way to describe the system. For example less parameters than in hydrodynamic calculations are necessary. Blast-wave models are used to describe transverse momentum spectra (dN/dp_{T}) and elliptic flow (v_2) data measured in heavy ion collisions to extract information about the freeze-out temperature and collective behavior of the QGP. In the following sections the temperature T and T_{kin} are used equivalent, both denotes the kinetic freeze-out temperature.

Tab. 2 provides an overview of some blast-wave models introduced in the following. The first description of transverse momentum spectra by a blast-wave model was done in 1993 by Schnedermann et al. [22]. They considered central collisions at mid-rapidity which corresponds to a solid cylindrical source geometry. The free parameters were the temperature and the radial flow strength which is assumed to be zero in the center of the cylinder and maximal on its edge. In [18] this model was generalized by considering non central collisions. An additional parameter ρ_{a}, which takes the azimuthal momentum space anisotropy (elliptic flow) into account, was introduced. Based on the previous descriptions, the STAR collaboration added a fourth parameter s_2, which corresponds to the spatial anisotropy of the freeze-out surface [17]. A factor $1 + 2s_2 cos(2\phi_{\mathrm{b}})$ was added to the formula of v_2. For a good agreement with the data, it was necessary to include the additional parameter $s_2 \neq 0$ and the azimuthal velocity variations described in [18]. Note that, $s_2 = 0$ corresponds to a spatially isotropic freeze-out surface.

A further blast-wave model with eight free parameters were used in [23]. An elliptical freeze-out distribution in transverse direction (x-y plane) is assumed there. The two parameters R_x and R_y are the radii of this ellipse.

In this bachelor thesis the blast-wave model which is provided in [24] is used. The elliptic flow v_2 and dN/dp_{T} data are fitted simultaneously in this model to extract the kinetic freeze-out temperature and the radial flow velocity. The particle yield is calculated with equation 3 where I_0 and K_1 are modified Bessel functions and $m_{\mathrm{T}} = \sqrt{m^2 + p_{\mathrm{T}}^2}$ the transverse mass. The elliptic flow v_2 is given by equation 4 where I_2 is a Bessel function too. The derivation follows the Cooper-Frye freeze-out formula and is shown in [24].

$$\frac{1}{2\pi p_{\mathrm{T}}} \frac{\mathrm{d}N}{\mathrm{d}p_{\mathrm{T}}\mathrm{d}y} \propto m_{\mathrm{T}} \int_0^1 \hat{r}\mathrm{d}\hat{r} \int_0^{2\pi} \mathrm{d}\hat{\phi}\, I_0(\xi_p) K_1(\xi_m), \tag{3}$$

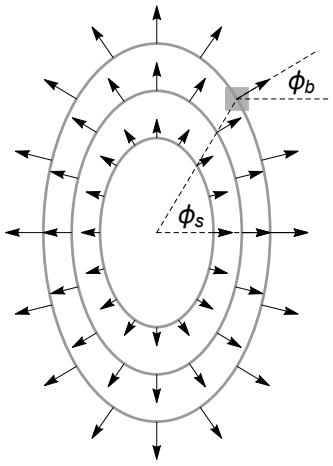

Figure 3: Elliptical freeze-out surface with radii R_x and R_y. The angle ϕ_s points in the direction of the considered cell and ϕ_b represents the boost vector, which is assumed to be perpendicular to the surface. In general $\phi_\mathrm{b} \neq \phi_\mathrm{s}$. Figure taken from [24].

$$\xi_\mathrm{p} \equiv \xi_\mathrm{p}(\hat{r}, \hat{\phi}) = \frac{p_\mathrm{T} \sinh \rho(\hat{r}, \hat{\phi})}{T},$$
$$\xi_\mathrm{m} \equiv \xi_\mathrm{m}(\hat{r}, \hat{\phi}) = \frac{m_\mathrm{T} \cosh \rho(\hat{r}, \hat{\phi})}{T}$$

$$v_2(p_\mathrm{T}) = \frac{\int_0^1 \hat{r}\mathrm{d}\hat{r} \int_0^{2\pi} \mathrm{d}\hat{\phi}\, I_2(\xi_\mathrm{p}) K_1(\xi_\mathrm{m}) \cos(2\phi_\mathrm{b})}{\int_0^1 \hat{r}\mathrm{d}\hat{r} \int_0^{2\pi} \mathrm{d}\hat{\phi}\, I_0(\xi_\mathrm{p}) K_1(\xi_\mathrm{m})}. \tag{4}$$

The free parameters in this blast-wave model are the temperature T, ρ_0 and ρ_2 (corresponds to ρ_a in [17]) and the radii ratios of R_x and R_y of the elliptical freeze-out surface. In contrast to [17] the spatial anisotropy is included by considering an elliptical freeze-out surface, shown in Fig. 3, and not by including $s_2 \neq 0$. The boost vector of the fluid cell is assumed to be perpendicular to this elliptical surface and in general $\phi_\mathrm{b} \neq \phi_\mathrm{s}$. The transverse rapidity with the azimuthal modulation (ρ_2) is given by equation 5. The transverse velocity β_T can be calculated with $\beta_\mathrm{T} = tanh(\rho)$ and is related to the velocity on the surface β_s ($\hat{r} = 1$) by equation 6. The mean flow velocity follows with equation 7, where $n = 1$ for a linear increase of the flow velocity from the center to the surface. In the following sections the mean transverse velocity is denoted as $\langle\beta\rangle$.

$$\rho \equiv \rho(\hat{r}, \hat{\phi}) = \hat{r}\,(\rho_0 + \rho_2 \cos(2\phi_\mathrm{b})) \tag{5}$$

$$\beta_\mathrm{T}(r) = \beta_\mathrm{s} \left(\frac{r}{R}\right)^n \tag{6}$$

$$\langle\beta_\mathrm{T}\rangle = \tanh(\langle\rho\rangle) = \tanh\left(\frac{2}{n+2} \cdot \left(\rho_0 + \rho_2 \frac{1 - R_x/R_y}{1 + R_x/R_y}\right)\right) \tag{7}$$

A modified blast-wave model, based on Monte-Carlo simulations, will be provided in an additional paper [25]. It is assumed that the momenta of the particles within the fluid cell are Boltzmann distributed and the cell is boosted in the direction of ϕ_b. The formulas for the particle yield and elliptic flow are given in the appendix A.1.

While light (u, d, s) quarks are thermalized in the QGP, the behavior of heavy (c and b) quarks

is still uncertain. In order to receive indications about a possible thermalization of heavy quarks in the QGP, the blast-wave model described above was used to simultaneously fit spectra and elliptic flow data at LHC energies in [24]. At LHC energies the behavior of the bottom quark is studied by including spectra and elliptic flow data of the Υ. No disagreement of the Υ data with the blast-wave model was found. Further investigations about a possible thermalization and the collective behavior of heavy quarks are carried out in this bachelor thesis. Simultaneous blast-wave fits to spectra and elliptic flow data measured in Au+Au collisions at $\sqrt{s_{\mathrm{NN}}} = 200$ GeV are performed. At this lower energy the focus is on the behavior of the charm quark instead of the bottom quark. Due to their quark content the D^0 and J/ψ mesons are studied.

Table 2: Overview and comparison of hydrodynamic and blast-wave models.

		Blast-wave		
	Hydrodyn.	Schnedermann et al. [22]	STAR [17]	Reygers and Schmah [24]
Free parameters	T, P, ϵ, s, η/s	T, β_s	T, ρ_0, ρ_a, s_2	T, ρ_0, ρ_2, R_x/R_y
Assumptions	Local thermodynamic equilibrium	Boost-inv. longitudinal flow	Boost-inv. longitudinal expansion	Certain flow velocity at the freeze-out coordinates
	Initial conditions, e.g. Glauber model		Azimuthal velocity variations (ρ_a)	Azimuthal velocity variations (ρ_2)
	Transition QGP to hadron gas: Cooper-Frye ansatz			Particles stream directly to the detector after the freeze-out (neglect resonance decays)
Spatial anisotropy		-	Factor $(1 + 2s_2 cos(\phi_\mathrm{b}))$ $s_2 \neq 0$	Elliptical freeze-out surface
Special features	3-dimensional models			Simultaneous fit to dN/dp_T and v_2

1.3 Outline

One part of this bachelor thesis provides a variety of spectra and elliptic flow (v_2) data usable for the main program to carry out the blast-wave fits. For that it is necessary to convert the available data into a unified format. In section 2.1 the procedure of this conversion is described. The main program which is used to perform the blast-wave fits already exists. Only the method for importing data is changed in a way that adding new data and selecting data for the fits becomes very easy. These modifications are described in section 2.2. Spectra and elliptic flow data measured in Au-Au collisions at 7.7, 11.5, 14.5, 19.6, 27, 39, 62.4 and 200 GeV taken at RHIC are used. In addition 2.76 and 5.02 TeV data measured in Pb-Pb collisions at CERN LHC are included.

Fits to high energy data are carried out in section 3. Fits to $\sqrt{s_{\mathrm{NN}}} = 2.76$ TeV data, which were already done in [24], are reproduced first in section 3.1 for the verification of the program. The analysis of the $\sqrt{s_{\mathrm{NN}}} = 5.02$ TeV data follows. Results, which are presented in [26], with included feed-down calculations and the boost model for $\sqrt{s_{\mathrm{NN}}} = 2.76$ TeV are briefly shown in section 3.2.

In section 3.3 the systematic study of the fits to spectra and elliptic flow data at $\sqrt{s_{\mathrm{NN}}} = 200$ GeV follows. As already mentioned the possibility of the thermalization of heavy quarks is investigated. Various fit ranges and particles are used for the fits as well as different collision centralities.

After that a standard fit to K, p and Λ spectra and elliptic flow data is carried out for all energies of the Beam Energy Scan program to investigate the behaviour of the freeze-out temperature and the mean flow velocity at the full energy range from $\sqrt{s_{\mathrm{NN}}} = 7.7$ GeV - 5.02 TeV.

For the following data analysis the CERN ROOT framework was used [27]. It is based on C++ and provides different possibilities for the statistical analysis and for mathematical calculations. The visualization and saving of huge amounts of data is realized. Different objects like histograms or graphs can be created and tools for fitting functions are provided.

2 Data converting and importing tools

2.1 Converting data

In this section the tool which is used to convert data is described. The conversion of the data into a unified format is necessary because the fit program can only handle one data format and always assumes dN/dp_{T} or v_2 as function of p_{T}. Variations like $1/p_{\mathrm{T}} \cdot dN/dp_{\mathrm{T}}$, dN/dm_{T} or different error types were given in the data files. Today it is standard to upload data together with a paper on the HEP webpage [28]. From this site the data can be downloaded in different formats, for example as ROOT files, which are used here. Some collaborations still provide their data in text files. The purpose of the tool described in this section is to convert such ROOT files from the HEP site and text files into a format which can be used for the fit program. The created outputs are ROOT objects with clearly defined titles, consisting of the particle identification, the energy and the corresponding centrality. The x-value is always the transverse momentum p_{T} in GeV/c and the y-value is either v_2 or dN/dp_{T} with arbitrary normalization and the possibility of having an absolute normalization later on. This generalization simplifies the importing and selection of the data which is used for the blast-wave fits in the main program. This is described in more detail in the next section 2.2.

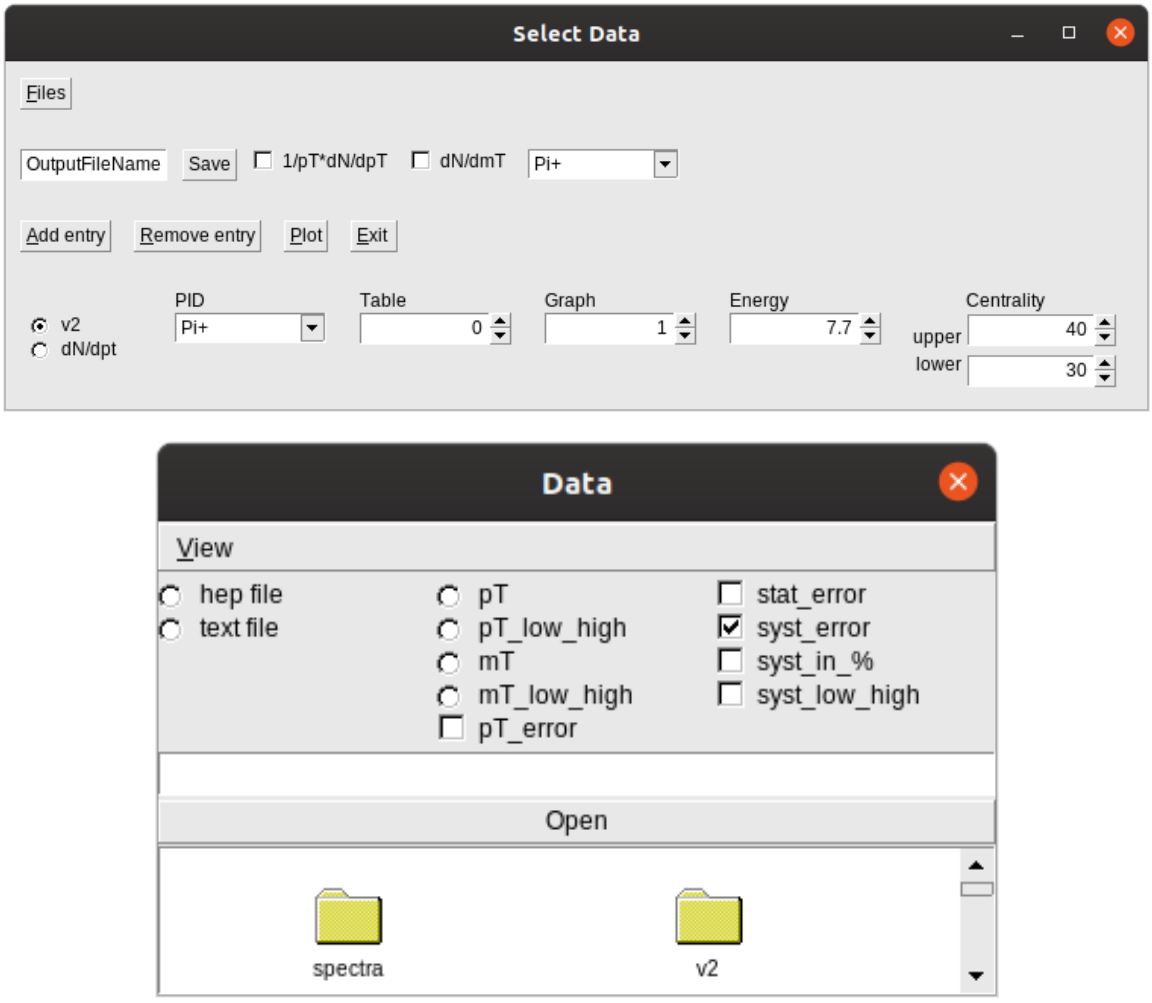

Figure 4: Upper: Main frame of the GUI. The bottom row shows the entries for creating the titles if the input file was a ROOT file. Lower: Second Frame of the GUI used to select the input file and specify the text file.

The selection of the input file and several information is done with a GUI (graphical user interface). The two frames of this GUI are shown in Fig. 4.

Every conversion starts with selecting the *"Files"* text button in the main frame. The second frame opens (Fig. 4 lower part) which contains a window with the local file and some check boxes on the top. The input file (ROOT files from the HEP site or text files) can be selected and with double clicking on it, it is displayed in the text entry. In the first column of check boxes the selected kind of file can be marked.

The other check boxes are used for a given input text file, because a specification of the text file in more detail is necessary. The given x- and y-values and uncertainties for the different particle spectra or v_2 data are not always equal. First it is possible to choose between a given mean p_{T} or m_{T} value (*"pT"* or *"mT"* check button) or a p_{T} or m_{T} bin (*"pT_low_high"* or *"mT_low_high"* check button) in the second column of check boxes. It is only possible to click one of this four check buttons at the same time. In the case of a given mean p_{T} value with a p_{T}-error, the additional *"pT_error"* check box can be selected. The last column of check boxes contains different kinds of y-errors. If the check box for a systematic error is selected, two additional check boxes appear. It is possible to convert a systematic error given in percent to an absolute value (*"syst_in_%"* check box) and handle the upper and lower bound of the systematic errors (*"syst_low_high"* check box). With the *"Open"* text button the file in the text entry will be opened.

After entering the output file name in the text entry and selecting the *"Save"* text button, a new ROOT file with the entered name is created. Right before saving, the function *"DoFillGraph()"* is called. This is the main function which creates the *TGraphAsymmErrors* out of the text file. The number of columns of the input text file is essential to get the input format. It is fixed after the *"Open"* text button is selected. The minimum number is three (x, y and statistical error) and the maximum number is six (lower x, upper x, y, statistical error, lower systematic error, higher systematic error). Fig 5 shows an example of a text file with a low and high p_{T} value, $1/p_{\mathrm{T}} \cdot dN/dp_{\mathrm{T}}$ with statistical and systematic errors.

The function *DoFillGraph()* takes every line of the input file separately. Every time there is a white space or a tab in the current line, the previous value is written into a vector. Different numbers of spaces and tabs are taken into account. The only item which needs to be added are the identifiers between the data blocks, as shown in the example (Fig. 5). This means every time the particle, energy or centrality changes there should be an identifier with the following form:

#v2_PID_x_E_x_C_lower_upper or #dNdpt_PID_x_E_x_C_lower_upper

where E is the energy and C the centrality. The used PIDs for the particles are listed in Tab. 3. It is very important that the identifiers do not differ, because they are used later in the main program. After one data block ends and the next identifier starts the values are saved in a *TGraphAsymmErrors* labeled with the identifier. There are always two graphs with the same titles, one with statistical and one with the systematic errors. If there is no systematic error it is set to zero. To indicate the errors the identifiers get the ending *"_stat"* or *"_syst"*.

Depending on the check boxes, which were selected before opening the file, some calculations are done. If *"mT"* is selected, p_{T} can be calculated with equation 8, where m is the mass of the particle.

$$p_{\mathrm{T}} = \sqrt{m_{\mathrm{T}}^2 - m^2} \tag{8}$$

$$\frac{dN}{dp_{\mathrm{T}}} = \frac{p_{\mathrm{T}}}{m_{\mathrm{T}}} \cdot \frac{dN}{dm_{\mathrm{T}}} \tag{9}$$

Next to the saving button there are some additional check boxes. By selecting *"1/pT*dN/dpT"* the given y-value is multiplied by p_{T}. It is $1/m_{\mathrm{T}} \cdot dN/dm_{\mathrm{T}} = 1/p_{\mathrm{T}} \cdot dN/dp_{\mathrm{T}}$ and thus the same check box is used if the input data is given in terms of m_{T}. A conversion of dN/dm_{T} to dN/dp_{T} is done if *"dN/dmT"* is selected. The calculation follows equation 9. Since the mass of the particle appears in equations 8 and 9, it is necessary to specify the particle type in the drop down menu next to the

check buttons. The saving process is finished, if *"# end of file"* appears in the text file (Fig. 5).

```
#dNdpt_PID_Pi-_E_7.7_C_0_5
0.25   0.30   114.898   0.21538   7.89015
0.30   0.35   83.9507   0.17051   5.61535
0.35   0.40   62.4481   0.13799   4.10800
0.40   0.45   46.3708   0.11247   3.01883
⋮
#dNdpt_PID_Pi-_E_7.7_C_5_10
0.25   0.30   97.6701   0.20042   6.70708
⋮
# end of file
```

Figure 5: Example of an input text file. From left to right: Low and high p_{T}, $1/p_{\mathrm{T}} \cdot dN/dp_{\mathrm{T}}$, statistical and systematic error. Lines which begin with "#" are used as identifier for the graphs.

For ROOT files from the HEP site the procedure is much simpler. Once the input file and the check button *"hep file"* are selected, the file can be opened without any additional selections. With clicking on *"Add entry"* text button, different check buttons (*"v2"*, *"dN/dpt"*) and entries (*"PID"*, *"Table"* etc.) appear, already shown in the upper panel of Fig. 4. They are necessary to create the identifier, which was written in the text file before. After the selection of the particle, energy, centrality, table and graph number the data can be plotted with the *"Plot"* text button. It is possible to add at maximum nine entries, where one can remove any with the *"Remove entry"* text button. The check buttons next to *"Save"* work basically the same as in the case of an input text file. This time the function *DoFillGraph()* only takes the selected table and graph out of the ROOT file to create the *TGraphAsymmErrors*. A second function *DoFillHistName()* creates the identifiers out of the selected information.

The used particles and their corresponding quark contents and masses are listed in Tab. 3. The converted data are listed in Tab. 4 and Tab. 5. Only the centralities (central, mid-central and peripheral) used for the fits in the next sections are listed here. For some particles at some energies are more centralities available. The data is stored in a directory which is uploaded to the GitHub repository. It will be then available for every user.

Table 3: Particles used in this thesis, their quark contents and masses [29] and the PIDs used for the identifiers.

Particle	**Quark content**	**Mass (MeV/c^2)**	**PID**
π^+, π^-	$u\bar{d}$, $\bar{u}d$	139.57	Pi+, Pi-
K^+, K^-	$u\bar{s}$, $\bar{u}s$	493.68	K+, K-
p, $\bar{p}$	uud, $\bar{u}\bar{u}\bar{d}$	938.27	P, Pbar
ϕ	$s\bar{s}$	1019.46	Phi
Ξ^-, $\bar{\Xi}^+$	dss, $\bar{d}\bar{s}\bar{s}$	1321.71	Xi-, Xibar+
Ω^-, $\bar{\Omega}^+$	sss, $\bar{s}\bar{s}\bar{s}$	1672.45	Omega-, Omegabar+
Λ, $\bar{\Lambda}$	uds, $\bar{u}\bar{d}\bar{s}$	1115.68	Lambda, Lambdabar
K^0_s	$\frac{1}{\sqrt{2}}(d\bar{s} - s\bar{d})$	497.61	K0S
D^0	$\bar{u}c$	1864.83	D0
J/ψ	$c\bar{c}$	3096.90	J/Psi
Υ	$b\bar{b}$	9460.30	Upsilon
d, $\bar{d}$	p(uud)n(udd),	1875.61	d, dbar
He_3, $\overline{He_3}$	p,p,n	2808.88	He3, He3bar
t	p,n,n	2808.9	t
Λ_c	udc	2286.46	LambdaC

Table 4: Used elliptic flow (v_2) and dN/dp_{T} data at $\sqrt{s_{\mathrm{NN}}} = 5.02, 2.76$ TeV and $\sqrt{s_{\mathrm{NN}}} = 200$ GeV.

		Cent.(%)				**Cent.(%)**		
PID	**v_2 ref.**	**central**	**mid-c.**	**peri.**	**dN/dp_{T} ref.**	**central**	**mid-c.**	**peri.**
				$\sqrt{s_{\mathrm{NN}}}$ **= 5.02 TeV**				
$\boldsymbol{\pi}$	[30]	0-5	30-40	60-70	[31]	0-5	30-40	60-70
K	[30]	0-5	30-40	60-70	[31]	0-5	30-40	60-70
p	[30]	0-5	30-40	60-70	[31]	0-5	30-40	60-70
$\boldsymbol{\phi}$	[30]	0-5	30-40	50-60	-	-	-	-
$\boldsymbol{\Lambda}$	[30]	0-5	30-40	60-70	-	-	-	-
$\mathbf{K_s^0}$	[30]	0-5	30-40	60-70	-	-	-	-
$\mathbf{J}/\boldsymbol{\psi}$	[32]	-	30-50	-	[33]	0-20	20-40	40-90
$\boldsymbol{\Upsilon}$	[34]	-	5-60	-	-	-	-	-
				$\sqrt{s_{\mathrm{NN}}}$ **= 2.76 TeV**				
$\boldsymbol{\pi}$	[35]	0-5	30-40	50-60	[36]	0-5	30-40	60-80
K	[35]	0-5	30-40	50-60	[36]	0-5	30-40	60-80
p	[35]	0-5	30-40	50-60	[36]	0-5	30-40	60-80
$\boldsymbol{\phi}$	[35]	10-20	30-40	50-60	[37]	0-5	30-40	60-80
$\boldsymbol{\Xi}$	[35]	0-5	30-40	50-60	[38]	0-10	20-40	60-80
$\boldsymbol{\Omega}$	[35]	5-10	30-40	50-60	[38]	0-10	20-40	60-80
$\boldsymbol{\Lambda}$	[35]	0-5	30-40	50-60	-	-	-	-
$\mathbf{K_s^0}$	[35]	0-5	30-40	50-60	-	-	-	-
$\mathbf{D^0}$	[39]	-	30-50	-	[40]	-	30-50	-
$\mathbf{J}/\boldsymbol{\psi}$	[41]	-	20-40	-	-	-	-	-
$\boldsymbol{\Upsilon}$	-	-	-	-	[42]	-	0-100	-
d	[43]	-	30-40	-	[44]	-	20-40	-
				$\sqrt{s_{\mathrm{NN}}}$ **= 200 GeV**				
$\boldsymbol{\pi}$	[45]	0-30	0-30	30-80	[46]	0-12	20-40	40-80
K	[45]	0-30	0-30	30-80	[47]	0-10	20-40	60-92
p	[45]	0-30	0-30	30-80	[46]	0-12	20-40	40-80
$\boldsymbol{\phi}$	[45]	0-30	0-30	30-80	[48]	0-10	20-30	70-80
$\boldsymbol{\Xi}$	[45]	0-30	0-30	30-80	[49]	-	20-40	-
$\boldsymbol{\Omega}$	[45]	0-30	0-30	30-80	[49]	-	20-40	-
$\boldsymbol{\Lambda}$	[45]	0-30	0-30	30-80	[49]	-	20-40	-
$\mathbf{K_s^0}$	[45]	0-30	0-30	30-80	[49]	-	20-40	-
$\mathbf{D^0}$	[50]	-	10-40	-	[51]	0-10	20-40	60-80
$\mathbf{J}/\boldsymbol{\psi}$	[52]	0-10	10-40	40-80	[53]	-	20-40	60-80
d	[54]	-	0-80	-	[55]	0-10	20-40	60-80
$\mathbf{He_3}$	[54]	-	0-80	-	-	-	-	-
t	[54]	-	0-80	-	-	-	-	-
$\boldsymbol{\Lambda_c}$	-	-	-	-	[56]	-	10-80	-

Table 5: Used elliptic flow (v_2) and dN/dp_{T} data at at $\sqrt{s_{\mathrm{NN}}}$ = 7.7, 11.5, 14.5, 19.6, 27, 39 and 62.4 GeV.

		Cent.(%)				**Cent.(%)**		
PID	**v_2 ref.**	**central**	**mid-c.**	**peri.**	**dN/dp_{T} ref.**	**central**	**mid-c.**	**peri.**
				$\sqrt{s_{\mathrm{NN}}}$ **= 62.4 GeV**				
π	[57]	0-10	10-40	40-80	[46]	0-10	20-40	40-80
K	[57]	0-10	10-40	40-80	[58]	0-5	30-40	70-80
p	[57]	0-10	10-40	40-80	[46]	0-10	20-40	40-80
ϕ	[57]	0-20	20-40	60-80	[48]	0-10	20-30	70-80
Ξ	[57]	0-10	10-40	40-80	[59]	0-5	20-40	60-80
Ω	[57]	0-10	10-40	40-80	[59]	0-20	20-40	40-60
Λ	[57]	0-10	10-40	40-80	[59]	0-5	30-40	60-80
K^0_s	[57]	0-10	10-40	40-80	[59]	0-5	20-40	60-80
J/ψ	-	-	-	-	[60]	0-20	20-40	40-60
d	[54]	-	0-80	-	[55]	0-10	20-40	60-80
He_3	[54]	-	0-80	-	-	-	-	-
t	[54]	-	0-80	-	-	-	-	-
				$\sqrt{s_{\mathrm{NN}}}$ **= 39 GeV**				
π	[57]	0-10	10-40	40-80	[61]	0-5	30-40	70-80
K	[57]	0-10	10-40	40-80	[61]	0-5	30-40	70-80
p	[57]	0-10	10-40	40-80	[61]	0-5	30-40	70-80
ϕ	[57]	0-20	20-40	60-80	[62]	0-10	30-40	60-80
Ξ	[57]	0-10	10-40	40-80	[63]	0-5	30-40	60-80
Ω	[57]	0-10	10-40	40-80	[62]	0-10	0-40	-
Λ	[57]	0-10	10-40	40-80	[63]	0-5	30-40	60-80
K^0_s	[57]	0-10	10-40	40-80	[63]	0-5	30-40	60-80
J/ψ	-	-	-	-	[60]	0-20	20-40	40-60
d	[54]	-	0-80	-	[55]	0-10	20-40	60-80
He_3	[54]	-	0-80	-	-	-	-	-
t	[54]	-	0-80	-	-	-	-	-
				$\sqrt{s_{\mathrm{NN}}}$ **= 27, 19.6, 11,5, 7,7 GeV**				
π	[57]	0-10	10-40	40-80	[61]	0-5	30-40	70-80
K	[57]	0-10	10-40	40-80	[61]	0-5	30-40	70-80
p	[57]	0-10	10-40	40-80	[61]	0-5	30-40	70-80
ϕ	[57]	0-20	20-40	60-80	[62]	0-10	30-40	60-80
Ξ	[57]	0-10	10-40	40-80	[63]	0-5	30-40	60-80
Ω	[57]	0-10	10-40	40-80	[62]	0-10	0-40	-
Λ	[57]	0-10	10-40	40-80	[63]	0-5	30-40	60-80
K^0_s	[57]	0-10	10-40	40-80	[63]	0-5	30-40	60-80
d	[54]	-	0-80	-	[55]	0-10	20-40	60-80
He_3	[54]	-	0-80	-	-	-	-	-
t	[54]	-	0-80	-	-	-	-	-
				$\sqrt{s_{\mathrm{NN}}}$ **= 14.5 GeV**				
π	[57]	0-10	10-40	40-80	[64]	0-5	30-40	70-80
K	[57]	0-10	10-40	40-80	[64]	0-5	30-40	70-80
p	[57]	0-10	10-40	40-80	[64]	0-5	30-40	70-80
Λ	[57]	0-10	10-40	40-80	-	-	-	-
K^0_s	[57]	0-10	10-40	40-80	-	-	-	-

2.2 Importing data to the main program

With the program described in the previous section it is now possible to create ROOT objects for v_2 and dN/dp_{T} data with clearly defined titles. For the further use, each of the created output files should be stored in a directory "Out". The next step was importing this data into the main program used for the blast-wave fits.

The previous functions for importing the data are replaced by a new one called *"load_data()"*. This function is called after starting the program. Every ROOT file in the directory "Out" is opened and the graphs within the files are stored in the vector *"vec_tgae"*. The identifiers of the graphs are stored simultaneously in the vector *"vec_tgae_name"*. The identifiers without the ending *"_stat"* or *"_syst"* are saved in *"vec_tgae_name_full"* and the error types are stored separately in the vector *"vec_error_type"*. In addition to that six two dimensional vectors are needed, three for v_2 and three for dN/dp_{T}. The first dimension always contains the particle identification (PID) and the second one the available energy, upper or lower centrality for every particle. Those vectors are labeled *"vec_pid_energy, vec_pid_cent_upper, vec_pid_cent_lower"*. They are used to handle the selection of particles for the fit.

The selection of the data and other settings for the fit is done with the GUI, shown in Fig. 6. The GUI was expanded by some particles (Ξ, Λ, $\mathrm{K}^0_{\mathrm{s}}$, He_3, t and Λ_c) and by separate check boxes for v_2 and dN/dp_{T}. They are necessary, because the available centralities are not always equal for both v_2 and dN/dp_{T}. The vectors, described above, are now used to manage the selection. With the two common drop down menus on the top of the check boxes the energy and centrality can be set for all particles. All available particles become green, the other ones red. At the same time the corresponding identifiers for the available particles are stored in a separate vector *"vec_tgae_id_{v2/dNdpt}_{fit/plot}"*. Every time this selection is repeated the vectors are reset and the new selection is saved. In addition to that it is possible to select every particle separately with the *"set"* check boxes below the particles. An additional frame with drop down menus for the energy and centrality for the corresponding particle opens. The identifier of the particle at the selected energy and centrality is added to the vector introduced before. In this vector a particle can only appear once. If there is already an identifier created with the selected particle but different energy or centrality, it is replaced by the new one.

Now, after the selection is finished, there are two vectors (one for v_2 and one for dN/dp_{T}) with the selected identifiers stored inside. The corresponding data can be plotted with selecting the *"Plot data"* text button. To get the right graphs, the identifiers in *"vec_tgae_id_{v2/dNdpt}_plot"* are compared to those in the vector *"vec_tgae_name_full"*. This gives the index under which the searched graph is stored in *"vec_tgae"*. Two canvases are opened for v_2 and dN/dp_{T}. It is necessary to click the check boxes in the *"PID plot"* frame, if the data should be plotted.

The two vectors *"vec_tgae_id_{v2/dNdpt}_fit"* are filled with identifiers used for the fit at the time of the selection. The fit starts with clicking on the red *"Minimize ana"* text button. Before that the fit ranges should be selected in the second frame of the GUI. This can be done for all particles at the same time using the entry on the top or for every particle separately.

After the fit is finished, the fit parameters with errors and the fit ranges can be saved in histograms with the *"Write params"* text button. The output file is a ROOT file. Its name consists of the selected energy, centrality and the particles used for the fit. Further specifications about the selected options for the fit can be added in the text entry.

This new selection and importing method offers several advantages. It is possible to add easily as much data as needed to the directory "Out" without changing anything in the program, as long as the identifiers have the correct shape. The selection is always done via the GUI and it is not necessary to read in data files separately. An additional particle can be added easily too, by including its mass and changing the number of particles. Conflicts may occur if an identifier appears twice. At the moment it is not possible to use data from different measurements/collaborations with same particles, energies and upper and lower centrality. One of the four parameters has to be different. A modification of the

selection method can be implemented to handle this issue in the future.

Figure 6: Main frame of the GUI which is used to select particles, energies and centralities for the blast-wave fits.

3 Blast-wave fits to v_2 and dN/dp_{T} data measured in high energy collisions

In this section simultaneous blast-wave fits to spectra and elliptic flow data measured in Pb-Pb collisions at $\sqrt{s_{\mathrm{NN}}} = 2.76$ and 5.02 TeV at the LHC are presented. For $\sqrt{s_{\mathrm{NN}}} = 2.76$ TeV a brief section about the fits with included feed-down calculations, which are carried out in [26], and fits with the boost model follows. In addition, a systematic analysis of fits to data measured in Au-Au collisions at $\sqrt{s_{\mathrm{NN}}} = 200$ GeV at RHIC are presented. It focuses on the question if heavy charm quarks are thermalized in the QGP. Fits with various collision centralities and different transverse momentum fit ranges and particles are carried out. The results from a fit with the standard blast-wave model is compared to the results obtained with the boost model.

3.1 Fit results for $\sqrt{s_{\mathrm{NN}}} = 2.76$ and 5.02 TeV

After changing the loading and selection method of the data used for the blast-wave fits, it was necessary to verify the program. The fits to spectra and elliptic flow data at $\sqrt{s_{\mathrm{NN}}} = 2.76$ TeV done in [24] are reproduced for this verification. The references of the used data are listed in Tab. 4.

After the particles, the centralities and the energy, which should be used for the fit, are selected, the fit range needs to be set. It is necessary to choose it carefully because at high p_{T} the jet contribution becomes more important. A maximum value for p_{T} is calculated with equation 10 [24], where m_0 is the rest mass of the particle, $\gamma^{\mathrm{max}} = 1/\sqrt{1-(\beta^{\mathrm{max}})^2}$ and $\beta^{\mathrm{max}} = 0.68$ for the standard fit.

$$p_{\mathrm{T}}^{\mathrm{max}} = cm_0\gamma^{\mathrm{max}}\beta^{\mathrm{max}} + 1.0 \ GeV/c \tag{10}$$

The jets arise because of high p_{T} hadrons, generated at the initial hard scattering process of the collision. These hadrons do not contribute to the collective behavior of the QGP and can not be described by the blast-wave model. A two-component model will be implemented in the future to better describe the high p_{T} range.

After the selection the fit can be started with selecting the red *"Minimize ana"* text button. The chosen spectra and v_2 data are stored in separate vectors. The data points for every graph, which are within the selected fit range, are taken and the corresponding blast-wave v_2 values and invariant blast-wave yields are calculated. The χ^2 values are extracted using equation 11, where the sum extends over every y-value within the fit range. From the graph y_i^{data} and y_i^{error} are extracted and y_i^{BW} is calculated with the fit function.

$$\chi^2 = \sum_i^n \frac{(y_i^{\mathrm{data}} - f_a \cdot y_i^{\mathrm{BW}})^2}{(y_i^{\mathrm{error}})^2} \tag{11}$$

It is necessary to include the scaling factor f_a for particle spectra because the invariant yield, which is obtained from the fit function, needs to be normalized to the data. Note that the scaling factor is equal to 1 for the calculations of v_2. The scaling factor can be obtained by calculating the minimum of equation 11 as function of the scaling factor f_a ($\frac{d\chi^2}{df_a} = 0$). This results in equation 12 for f_a.

$$f_a = \frac{\sum_i \frac{y_i^{\mathrm{data}} \cdot y_i^{\mathrm{BW}}}{(y_i^{\mathrm{error}})^2}}{\sum_i \left(\frac{y_i^{\mathrm{BW}}}{y_i^{\mathrm{error}}}\right)^2} \tag{12}$$

The minimization of the χ^2 value is done with Minuit and the Migrad algorithm [65]. It extracts the best fit parameters of T_{kin}, ρ_0, ρ_2 and R_x/R_y and the corresponding errors. A typical minimization

takes about five minutes.

The recent results of the simultaneous blast-wave fits (black) and the results of [24] (blue) are listed in Tab. 6. The results of the standard fit to K, p, ϕ and Ω at mid-centrality are in a good agreement with the previous fit results. The parameters T_{kin}, ρ_2 and R_x/R_y differ less than one sigma and ρ_0 is within the two sigma range. The significant change of the fit parameters by including the pions to the fit is reproduced too. Except ρ_2, which is within the three sigma range, all parameters differ less than one sigma. Because the same data, the same fit ranges and start parameters were used, actually no deviation is expected. We assume that the minor discrepancies originate from the different ROOT versions, which might have differences in the Minuit fitting algorithm.

Table 6: Current results of the blast-wave fits (black) compared to the results of [24] (blue) at $\sqrt{s_{\mathrm{NN}}} = 2.76$. The results for the fit at $\sqrt{s_{\mathrm{NN}}} = 5.02$ TeV are listed in the last line.

PID	**Comment**	$\boldsymbol{T_{\mathrm{kin}}}$ **(MeV)**	$\boldsymbol{\rho_0}$	$\boldsymbol{\rho_2}$	$\boldsymbol{R_x/R_y}$
		Fit results of [24]			
K, p, ϕ, Ω	$\beta^{\max} = 0.68$	128.4 ± 5.1	1.05 ± 0.01	0.09 ± 0.004	0.83 ± 0.004
K, p, ϕ, Ω, π	$\beta^{\max} = 0.68$	109.3 ± 2.2	1.11 ± 0.01	0.077 ± 0.002	0.83 ± 0.003
		Fit results of this bachelor thesis			
K, p, ϕ, Ω	$\beta^{\max} = 0.68$	126.8 ± 5.7	1.07 ± 0.01	0.094 ± 0.005	0.83 ± 0.004
K, p, ϕ, Ω, π	$\beta^{\max} = 0.68$	110.1 ± 2.2	1.11 ± 0.01	0.085 ± 0.003	0.83 ± 0.003
		Standard fit used in this bachelor thesis, $\sqrt{s_{\mathrm{NN}}} = 2.76$ TeV			
K, p, ϕ, Λ	$\beta^{\max} = 0.68$ mid-central	127 ± 4.6	1.07 ± 0.01	0.097 ± 0.004	0.83 ± 0.003
		Standard fit used in this bachelor thesis, $\sqrt{s_{\mathrm{NN}}} = 5.02$ TeV			
K, p, ϕ, Λ	$\beta^{\max} = 0.68$ mid-central	112.6 ± 3.2	1.15 ± 0.01	0.095 ± 0.003	0.85 ± 0.002

For the analysis in this bachelor thesis a standard fit to K, p, ϕ and Λ at mid-centrality is used. Note that at $\sqrt{s_{\mathrm{NN}}} = 2.76$ TeV only the spectra of K, p and ϕ are available. The fit range is calculated using equation 10 with $\beta^{\max} = 0.68$. The results of this standard fit, given in Tab. 6, are in a good agreement with the results of the K, p, ϕ and Ω fit.

The upper panel of Fig. 7 shows the fit results (solid lines) and predictions (dashed lines) for the v_2 data. The predictions are calculated with the results from the fit to other particles with the mass as free parameter.

For a quantitative comparison of the predictions to the data, the relative χ^2/point values of two fits can be used. Due to the different p_{T} ranges used for the fits we have to normalize the χ^2 to the number of fitted points in order to make a comparison between the fits possible. This can be done by multiplying equation 11 with $1/n$, where n is the number of fitted points in the selected fit range. We do not use the absolute values of χ^2/point because they are only useful if statistical errors are considered, which are gaussian distributed. In our case the statistical and systematic uncertainties are added quadratically. Further problems are the feed-down and jet contribution which prevent an exact description of the data.

As already seen in [24], the data in Fig. 7 is well described by the fit results and predictions. In addition the v_2 data of Λ, Ξ and $\mathrm{K}^0_{\mathrm{s}}$ are shown. The Λ baryon was included to the fit, which agrees well with the data. Within the fit range the deviations of the elliptic flow data to the predictions for the D^0 and J/ψ mesons are smaller than one sigma. A description of the zero v_2 of the Υ is still possible by the blast-wave model, but should only be taken as an upper limit due to the higher beam energy ($\sqrt{s_{\mathrm{NN}}} = 5.02$ TeV) [24].

The lower panel of Fig. 7 depicts the results of the simultaneous blast-wave fit for particle spectra, which are normalized to their integrals. The spectra of K, p and ϕ are in a good agreement with the fit curves. As expected due to feed-down effects, the pion spectra is much larger than predicted by the

blast-wave model. Because pions are the lightest hadrons they are produced the most in resonance decays. This is the reason why we do not include them to the fits [24]. The predicted spectra of the other particles are all within one or two sigma range of the data. The Ξ spectra is added here and can also be described by the fit prediction. Because the Υ is only available at 0-100%, it can not be compared to the prediction, which is done for mid-centrality. Because of this different centrality range used for the Υ spectra and the v_2 data measured at a higher energy it can not be fully determined if the bottom quark is thermalized in the QGP. It was concluded in [24] that a thermalization of the bottom quark in the QGP might be possible because no disagreement of the data with the blast-wave model was found.

Fig. 8 shows the results of a fit to the spectra and the elliptic flow data measured at $\sqrt{s_{\mathrm{NN}}} = 5.02$ TeV. The data references can be found in Tab. 4. The fit is done at mid-centrality (30-40%) with the v_2 data of K, p, ϕ and Λ and the K and p spectra. The p_{T} range is calculated using equation 10 with $\beta^{\mathrm{max}} = 0.68$.

The results for the v_2 data are depicted in the upper figure, where the fit curves are represented by solid lines and the fit predictions by dashed lines. The fit results and predictions are in a good agreement with the v_2 data of all particles. All data points of the Υ v_2 are described by the fit prediction with deviations less than one sigma. The two data points of the J/ψ are also not in a disagreement with the prediction but the deviations are slightly larger.

The spectra of π, K, p and J/ψ are depicted in the lower part of Fig. 8. They are normalized to their integrals. While the K and p spectra are well described by the fit, the prediction for the pion spectra deviates at small p_{T} from the data. This was expected due to the feed-down effect by which the pions are influenced the most. For that reason the pions were excluded from the fits and their p_{T} range starts only at $p_{\mathrm{T}} = 0.4$ GeV/c. Within this range the deviations are smaller. While the first two data points of the J/ψ spectrum are in agreement with the blast-wave prediction, the third point is much lower than this curve. Reasons for the deviations could be the different centrality or the scaling factor by which the calculated invariant blast-wave yield is multiplied. The scaling factor is calculated with equation 12. The third point is not in the p_{T} range and thus not taken into account for the calculation. If it is included, it dominates the normalization because of the small error. Because the shape of the predicted curve does not agree with the data, it is possible that other physics needs to be included here.

The obtained fit parameters are listed in the last line of Tab. 6. The kinetic freeze-out temperature is smaller than for $\sqrt{s_{\mathrm{NN}}} = 2.76$ TeV while the flow velocity is larger which might be a result of the larger initial pressure and energy density at higher beam energies. The possible description of the Υ v_2 data by the blast-wave model might be an additional indication for the thermalization of the bottom quarks in the QGP.

In the next section further investigations of the fits at $\sqrt{s_{\mathrm{NN}}} = 2.76$ TeV with included feed-down calculations and the boost model follow.

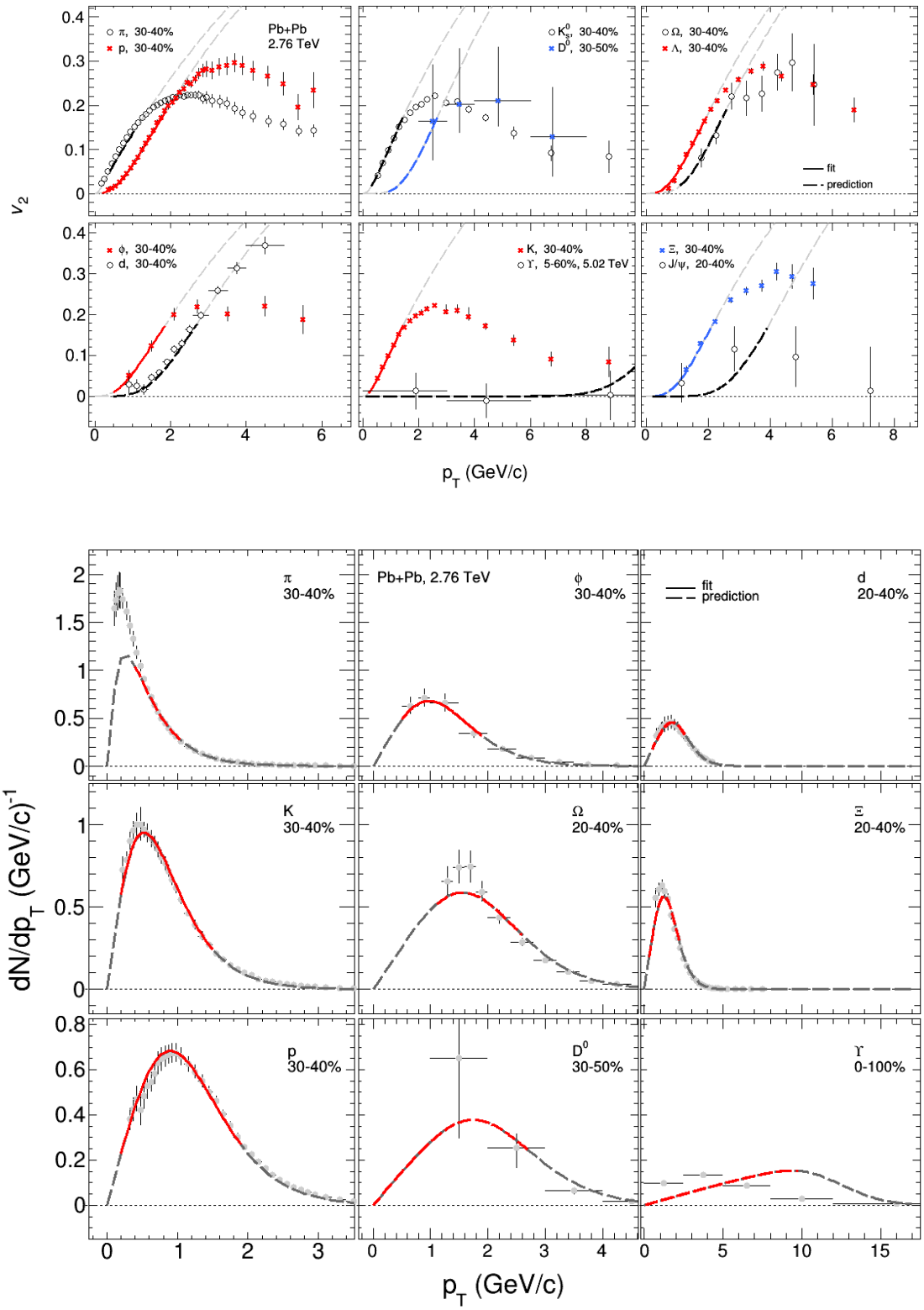

Figure 7: Simultaneous blast-wave fit results (solid lines) and predictions (dashed lines) for $\sqrt{s_{\rm NN}} = 2.76$ TeV. Upper: Results and predictions for the v_2 data. The ϒ elliptic flow was measured at $\sqrt{s_{\rm NN}} = 5.02$ TeV. Lower: Results and predictions for the spectra, which are normalized to their integrals.

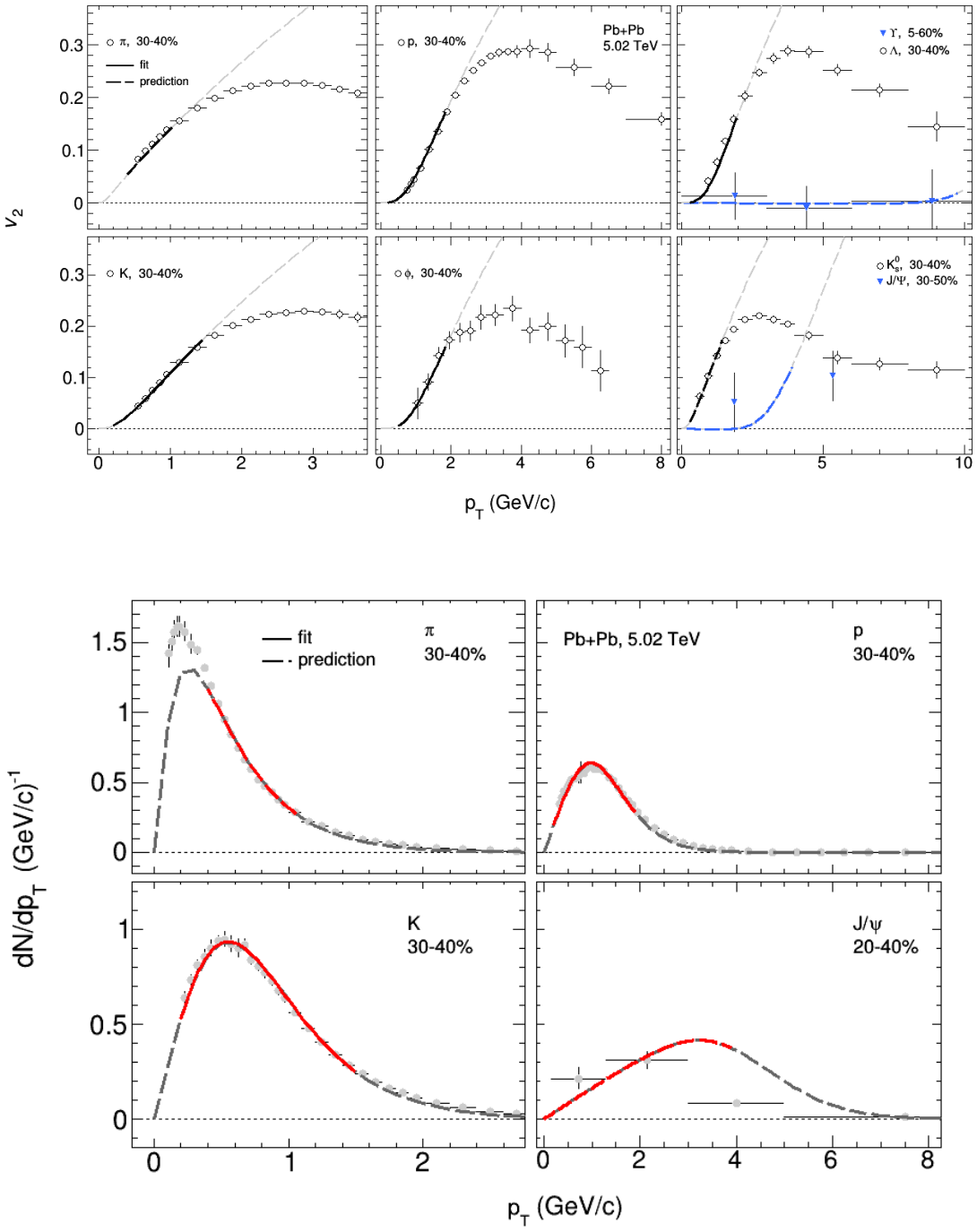

Figure 8: Simultaneous blast-wave fit results (solid lines) and predictions (dashed lines) for v_2 data (upper) and for particle spectra (lower) measured at $\sqrt{s_{\rm NN}} = 5.02$ TeV. All spectra are normalized to their integrals.

3.2 Feed-down

In this section fit results for $\sqrt{s_{\mathrm{NN}}} = 2.76$ TeV with included feed-down calculations, presented in [26], are shown. As already mentioned in section 1.2, it is assumed that the particles move directly to the detector after the freeze-out. In reality some of them decay into lighter particles before they reach the detector. This effect is called feed-down. The most particles produced in resonance decays are pions, because they are the lightest hadrons. Examples for such decays are $\eta \to \pi^+\pi^-\pi^0$, $\rho \to \pi\pi$ and $\Delta \to N\pi$.

To include this effect into the blast-wave model the feed-down contribution is calculated with a statistical model. The decay kinematics are included with Pythia. More details of the calculations and results with included feed-down are shown in another bachelor thesis [26].

Fig. 9 depicts the results for fits to (π), K and p with included feed-down for the standard blast-wave model ("fos" = freeze-out hyper-surface) and for the boost model ("boost"). The "fos" model is derived by using the Cooper-Frye formalism while the "boost" model is equivalent to a Monte-Carlo simulation with a local thermalized fluid cell which is boosted according to ϕ_{b} and ρ [25]. Both models are used for a fit with and without the pions. For all particles, except the pions, small differences between the models and the fits with and without pions are observed. While for the pions all four curves are basically equal for higher p_{T} values, significant differences between the models are observed at lower p_{T}. The best description of the pion spectrum is obtained with the boost model and by including the pions to the fit. The deviations for the standard blast-wave model with included pions are larger. Basically the same results are obtained for the pion spectrum for both models by excluding them from the fits.

Because the impact for the other particles is small, we exclude the pions in the following and use the standard blast-wave model without feed-down calculations.

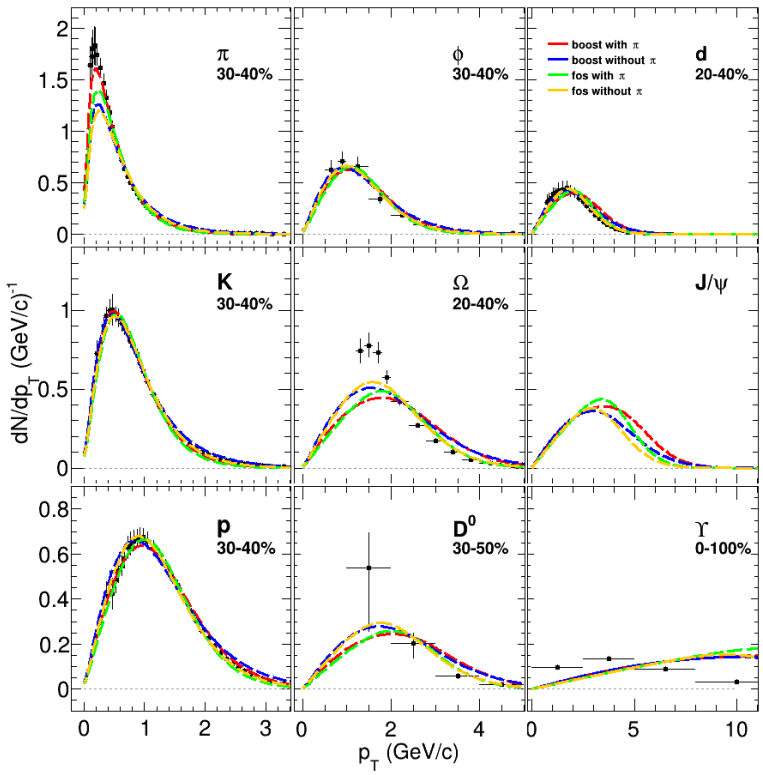

Figure 9: Simultaneous blast-wave fit results for the standard blast-wave and boost model with included feed-down calculations for the spectra measured at $\sqrt{s_{\mathrm{NN}}} = 2.76$ TeV. The spectra are normalized to their integrals. Figure taken from [26].

3.3 Systematic study of fits at $\sqrt{s_{\mathrm{NN}}} = 200$ GeV

In [24] simultaneous blast-wave fits at LHC energies were presented, focused on the question if heavy (charm and bottom) quarks thermalize in the QGP. This was done by including the spectra and elliptic flow data of J/ψ and Υ. With the same purpose simultaneous blast-wave fits to spectra and v_2 data are carried out at $\sqrt{s_{\mathrm{NN}}} = 200$ GeV in this bachelor thesis. In comparison to LHC energies the achieved energy density and temperature are lower at lower center-of-mass energies. Under these different initial conditions the behavior of the charm quark should be investigated, similar to the bottom quark at higher (LHC) energies. Due to their quark content the spectra and elliptic flow data of the D^0 ($\overline{\mathrm{u}}\mathrm{c}$) and J/$\psi$ ($\mathrm{c}\overline{\mathrm{c}}$) mesons are included. We intend to investigate the description of these mesons by a blast-wave model in order to get indications if heavy charm quarks are thermalized in the QGP or not. The spectra of the Λ_c baryon (udc) is also studied, but the corresponding v_2 data is not available.

In Tab. 4 the references of the used data, measured in Au-Au collisions at $\sqrt{s_{\mathrm{NN}}} = 200$ GeV, recorded at RHIC, are listed. The available centralities for v_2 and dN/dp_T are not always equal and in addition the centralities vary between the particles. For v_2 mostly 0-30% or 30-80% data are available (10-40% or 0-80% for the D^0 meson and only 0-80% for d, t and He_3), however for dN/dp_T the ranges are structured in steps of 10 or 20%. Basically three different centrality ranges are used; central, mid-central and peripheral, as described in Tab. 4. Because of this diversity, several fits with different particles and centralities, as well as slightly different fit ranges are considered.

Since at high p_T the jet contribution becomes more important, a maximum value for p_T is calculated with equation 10. The particles from jet fragmentation do not contribute to the collective behavior of the QGP and therefore they can not be described with the blast-wave model.

Because the spectra and elliptic flow measurements are influenced by the feed-down as described in section 3.2, the pions are excluded from the fits and the lower p_T limit needs to be chosen carefully. For the other hadrons all data points at low p_T are taken into account.

Tab. 7 gives an overview of the fitted particles, their centralities, the used fit ranges and the fit results. Because the differences of particle and anti-particle spectra and v_2 are very small at 200 GeV, they can be fitted simultaneously. A standard fit is done with K, p, ϕ and Λ, at mid-centrality, where the fit ranges are calculated with equation 10 and $\beta^{\max} = 0.68$. The results are shown in the first row of Tab. 7.

The same particles (K, p, ϕ and Λ) with the standard fit range ($\beta^{\max} = 0.68$) but other centralities are used for additional fits. The fit parameters for the most central collisions are almost the same as for mid-central ones, except the ρ_0. This was expected to some extent because the used centralities of the v_2 data are the same in both cases (0-30%). The radial flow velocity increases for more central collisions, because the pressure is most likely larger in this case. This is in agreement with the obtained ρ_0 values. Due to the larger spatial anisotropy in peripheral collisions, larger pressure difference in and out of the reaction plane, and thus a larger ρ_2 value is expected. Note that, ρ_2 describes the azimuthal anisotropy of the flow velocity. This is in agreement with the observation, where ρ_2 is about 1.4 times larger for the peripheral than for the most central collisions. Moreover R_x/R_y is closer to one for more central collisions than for peripheral collisions because of a more circular overlap zone. This is consistent with the fit results within the corresponding uncertainties. The freeze-out temperature is about 10% larger for peripheral collisions. The same effect with increasing freeze-out temperature for more peripheral collisions was observed in [58], where blast-wave fits to π, K and p spectra are presented. It should be noted that in the central and peripheral collisions, the spectra of the Λ baryon was not included, because it is only available at 20-40%. This can also influence the fit results.

For a systematic analysis the fit ranges are varied first to a lower and higher $\beta^{\max}$. The resulting fit parameters for $\beta^{\max} = 0.75$ are all within three sigma range compared to the parameters of the standard fit, except ρ_2 which deviates slightly more than three sigma. The deviation in the freeze-out

Table 7: Blast-wave fit results for $\sqrt{s_{\rm NN}} = 200$ GeV.

PID	**Comment**	$T_{\rm kin}$ **(MeV)**	ρ_0	ρ_2	R_x/R_y
		Standard fit			
K, p, ϕ, Λ	$\beta^{\rm max} = 0.68$ mid-central	128.6 ± 0.6	0.848 ± 0.002	0.048 ± 0.0003	0.91 ± 0.001
		Centrality variations			
K, p, ϕ, Λ	$\beta^{\rm max} = 0.68$ central	126.8 ± 0.7	0.847 ± 0.002	0.047 ± 0.0003	0.91 ± 0.001
K, p, ϕ, Λ	$\beta^{\rm max} = 0.68$ peripheral	141.9 ± 0.5	0.679 ± 0.002	0.068 ± 0.0003	0.77 ± 0.001
		Fit range variations			
K, p, ϕ, Λ	$\beta^{\rm max} = 0.75$ mid-central	128.9 ± 0.9	0.856 ± 0.003	0.047 ± 0.0002	0.91 ± 0.001
K, p, ϕ, Λ	$\beta^{\rm max} = 0.6$ mid-central	123.7 ± 0.7	0.866 ± 0.003	0.052 ± 0.0004	0.92 ± 0.001
		Particle variations			
K, p, ϕ, Ω	$\beta^{\rm max} = 0.68$ mid-central	130.4 ± 0.5	0.841 ± 0.0001	0.046 ± 0.0003	0.9 ± 0.001
K, p, ϕ, Λ, $\rm D^0$	$\beta^{\rm max} = 0.68$ mid-central	128.7 ± 0.6	0.847 ± 0.002	0.048 ± 0.0003	0.91 ± 0.001
K, p, ϕ, Λ, $\rm D^0$, π	$\beta^{\rm max} = 0.68$ mid-central	115.3 ± 0.3	0.893 ± 0.002	0.043 ± 0.0002	0.91 ± 0.0004
K, p, ϕ, Ξ, Ω, Λ, $\rm K^0_s$, $\rm D^0$, $\rm J/\psi$	$\beta^{\rm max} = 0.68$ mid-central	129.2 ± 0.6	0.845 ± 0.002	0.048 ± 0.0003	0.91 ± 0.001
		Results for the boost model			
K, p, ϕ, Ξ, Ω, Λ, $\rm K^0_s$, $\rm D^0$, $\rm J/\psi$	$\beta^{\rm max} = 0.68$ mid-central	129.6 ± 0.1	0.96 ± 0.002	0.058 ± 0.0002	0.89 ± 0.0004

temperatures is less than one sigma. With a smaller fit range with $\beta^{\rm max} = 0.6$ the differences become larger, due to less fitted data points.

In addition to the different centralities and fit range variations, different particles were included to the fits. The exchange of the Λ baryon by a Ω baryon had a very small effect on the fit parameters. Almost no deviations in the fit parameters of the standard fit is obtained by including the $\rm D^0$ meson. As already seen in [24] the largest impact on the fit parameters arises by including the pions to the fit. This leads to a temperature difference of about 13 MeV compared to the other fits at mid-centrality.

In [58] they obtained $T_{\rm kin} = 89 \pm 12$ MeV and a mean flow velocity of $\langle\beta\rangle = 0.592 \pm 0.051$ for 0-5%. By reproducing the fit with the same data and fit ranges, we obtain a temperature of $T_{\rm kin} = 89 \pm 0.1$ MeV and a flow velocity of $\langle\beta\rangle = 0.618 \pm 0.002$. This is within one sigma range.

By including all particles in the fit using the available spectra and v_2 data for mid-central events, almost the same fit parameters are obtained compared to the other results at mid-centrality. In addition the results of a fit with the boost model are shown in the last row of Tab. 7. In comparison to the fit with the standard blast-wave model to all particles at mid-centrality, the temperature is almost equal but for the other fit parameters we observe differences. We found a larger ρ_0 and ρ_2 for the boost model than for the standard model, which leads to a larger flow velocity if the fit is done with the boost model. The ratio R_x/R_y is smaller for the boost model.

Fig. 10 depicts the results of this simultaneous blast-wave fit to spectra and elliptic flow data of K, p, ϕ, Ξ, Ω, Λ, $\rm K^0_s$, $\rm D^0$ and $\rm J/\psi$. The upper panel shows the results (solid lines) and predictions (dashed lines) for the v_2 data for the standard blast-wave model. The corresponding results for the boost model are shown in the appendix, Fig. 16. The predictions are calculated with the obtained fit

parameters from fits to other particles where only the mass is left as a free parameter. If the data for particles and anti-particles are available separately, only the particle elliptic flow is shown because the v_2 data for the anti-particles are almost identical at $\sqrt{s_{\rm NN}} = 200$ GeV. The v_2 data is well described by the blast-wave predictions within the selected fit ranges. For higher $p_{\rm T}$ values the v_2 data reaches a constant value or decreases after a maximum. This high $p_{\rm T}$ range can not be described with the blast-wave predictions because the corresponding particles are dominantly from jet fragmentation. The jet particles do not contribute to the flow of the medium and especially have almost no elliptic flow.

In general the v_2 data of all particles are in good agreement with the fit and the predictions. The fitted particles are well described except some small deviations at low $p_{\rm T}$. The predictions for $\rm He_3$ and tritium deviate less than two sigma from the data. The v_2 of the deuteron is not in agreement with the fit prediction but for those three light nuclei (d, t, $\rm He_3$) only the full centrality range 0-80% is available and can not be fully compared to the prediction, which is for mid-centrality. This means deviations of the prediction from the data are expected.

The v_2 data of $\rm D^0$ and $\rm J/\psi$ can also be fairly described by the blast-wave model. The centrality for those two mesons is slightly different compared to that of the other particles which might be the reason for some deviations. The v_2 of the $\rm D^0$ meson measured in more central collisions is expected to become smaller, which would be in a better agreement with the prediction. The large v_2 value at low $p_{\rm T}$ for the $\rm J/\psi$ is not expected because, in general, the elliptic flow is increasing with increasing $p_{\rm T}$ until the jet contribution becomes important.

The lower panel of Fig. 10 shows the results of the simultaneous blast-wave fit for the particle spectra which are normalized to their integrals. Similar to the v_2 data, the anti-particles are not shown because they are almost identical to the particle spectra. The results for the standard blast-wave model ("fos") are shown in red and for the boost model ("boost") they are represented in blue. The fit results for the fitted particles are again represented by solid lines and the dashed lines show the fit predictions for every particle, in gray for the standard blast-wave model and in blue for the boost model. The normalization of the blast-wave fit curve to the data is done by multiplying the invariant blast-wave yield with a scaling factor which is obtained with equation 12.

A good agreement with the data is found for the fitted particles except some sizeable deviations of the $\rm D^0$ and $\rm J/\psi$. No significant deviations between the two models ("fos" and "boost") are observed for all particles, except for the pions at low $p_{\rm T}$. While for the higher $p_{\rm T}$ values both fit predictions are almost equal, the data is clearly better described by the boost model, compared to the standard model at lower $p_{\rm T}$, where the deviation is less than one sigma. The pions were always the particles which were not described by the standard model and thus they were excluded from the fits.

The results for $\rm K^0_s$, Ω and Ξ differ less than two sigma from the data. This implies that a simultaneous description of the light particles (π, K, p) and heavier particles such as Ω or Ξ might be possible. Only the deuteron spectrum is not in agreement with the data at low $p_{\rm T}$.

The behavior of the $\rm D^0$ and $\rm J/\psi$ mesons are of particular interest due to their heavy quark content. The spectra of the $\rm D^0$ meson is well described for $p_{\rm T} > 1.6$ GeV/c. At smaller $p_{\rm T}$ values the fit curve is lower than the data. The points deviate each about two sigma from the blast-wave prediction. The deviations might arise due to the scaling factor which is used to get the absolute values of the invariant blast-wave yield. The scaling factor is calculated with equation 12 out of the χ^2 which is weighted with the y-error. Because the y-errors are larger for the first three data points of the $\rm D^0$ spectrum, their influence on the result is minimal. Nevertheless a clear shape difference between data and blast-wave prediction is observed. Significant deviations are observed for the $\rm J/\psi$ too. Because the shapes of the fit curves differ from the data it is possible that other physics needs to be included here. As a cross check whether the fit results are dominated by low mass particles we also did a fit to $\rm K^0_s$, $\rm D^0$ and $\rm J/\psi$ data, measured in mid-central collisions, and with $\beta^{\rm max} = 0.68$. The results are shown in Fig. 17 in the appendix A.2. For this particular fit the $\rm D^0$ and $\rm J/\psi$ spectra are well described.

On the other hand particles like the proton showing now deviations to the blast-wave predictions. In addition, the predictions for v_2 do not agree with the data. The fit parameters are $T_{\mathrm{kin}} = 197.6 \pm 3.2$, $\rho_0 = 0.58 \pm 0.01$, $\rho_2 = 0.01 \pm 0.001$ and $R_x/R_y = 0.69 \pm 0.005$. Here the ρ_2 parameter is at the lower boundary and therefore further investigations are necessary.

Since there are only two data points of the spectra of the Λ_{c} baryon and the v_2 data is not available, it is not included to the discussions.

In [51] blast-wave fits to particle spectra are performed. They did fits to the lighter particles (π, K, p), the multi-strange particles (Ξ and ϕ) and the D^0 meson separately and observe that the D^0 behaves like the strange particles. Differences between the results from π, K, p and from the D^0 meson are interpreted as an earlier decoupling of the heavier particles from the system.

Because almost all particles can be described quite well in Fig. 10, one might expect that the multi-strange and light particles can not be distinguished regarding the freeze-out and their collective behavior. Deviations of the fit predictions to the data are already expected due to the mixed centrality ranges used for the fits. For better results v_2 data at mid-centrality (20-40% or 30-40%) should be used. In addition different centrality classes are used in the v_2 data for the D^0 and J/ψ mesons and for the other particles. Further investigations with better matching centralities and included feed-down calculations should be carried out in order to get more precise results.

Because the considered system is much more complex than assumed in the model, perfect predictions are not expected. On the other hand this is mostly also the case for hydrodynamic models. Nevertheless the blast-wave model provides a very good description of the spectra and v_2 data of almost all particles at $\sqrt{s_{\mathrm{NN}}} = 200$ GeV. The deviations between the blast-wave model and D^0 and J/ψ spectra data is quite significant. Therefore it seems that charms quarks might not fully thermalize in the QGP and additional physics is needed to describe their production and kinematic behaviour.

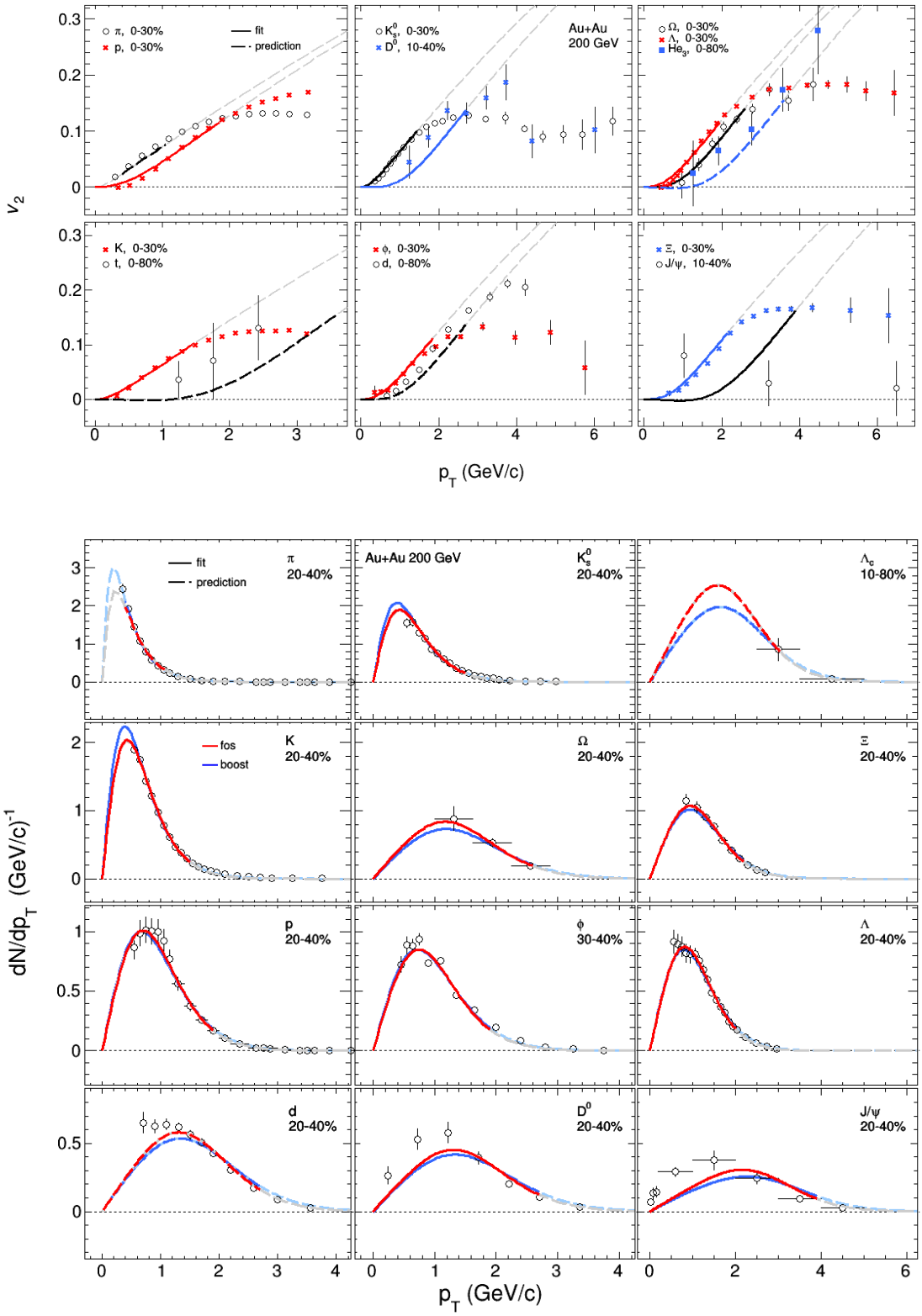

Figure 10: Simultaneous blast-wave fit results (solid lines) and predictions (dashed lines). Upper: Results for the v_2 data with the standard blast-wave model. The results for the boost model are shown in the appendix, Fig. 16. Lower: Results (red) and predictions (gray) for the spectra, obtained with the standard blast-wave model ("fos") and the boost model ("boost"), where results and predictions are shown in blue. The spectra are normalized to their integrals.

4 Energy dependence of the blast-wave parameters and fits to $\sqrt{s_{\mathrm{NN}}} = 7.7 - 62.4$ GeV

In this section simultaneous blast-wave fits to spectra and elliptic flow data at energies of the Beam Energy Scan (BES) program performed at RHIC are presented. In 2010/2011 data was recorded in Au-Au collisions at $\sqrt{s_{\mathrm{NN}}} = 7.7, 11.5, 19.6, 27, 39$ and 62.4 GeV at the STAR experiment. The data at $\sqrt{s_{\mathrm{NN}}} = 14.5$ GeV followed later in 2014 [57]. The idea of the BES program was to study the properties of the QGP by varying the center-of-mass energy of the colliding gold nuclei. The main goal was to receive information about the QCD phase transition and the critical point. Since the baryon chemical potential is changing at different beam energies, different areas of the phase diagram can be investigated.

In [12] differences between the v_2 values for particles and anti-particles were observed for the first time. This observation violated the expected NCQ (Number of Constituent Quarks) scaling which was found at $\sqrt{s_{\mathrm{NN}}} = 200$ GeV. Baryons consist of three quarks and get v_2 values which are up to a factor 1.5 larger than the v_2 values of the mesons. Because the thermalized quarks have all the same kinetic energy, the differences in v_2 between baryons and mesons after the freeze-out appear due to their number of valence quarks. In [19] a possible explanation is discussed. They assume a different elliptic flow for particles which consist of produced quarks and anti-quarks compared to quarks from the colliding incoming nucleons. The produced $\mathrm{q\overline{q}}$-pairs are fully thermalized in this model. Due to baryon stopping the quarks of the incoming nucleons are transported to mid-rapidity. They get a higher elliptic flow than the produced quarks due to more scatterings while they are transported to mid-rapidity [19]. Because the baryon stopping effect at mid-rapidity decreases with increasing beam energy there are no differences between particles and anti-particles for $\sqrt{s_{\mathrm{NN}}} = 200$ GeV, 2.76 or 5.02 TeV. At these higher energies the quarks of the incoming nucleons stay close to $y = y_{\mathrm{beam}}$ and are not transported to $y = 0$.

The left panel of Fig. 11 shows the found difference in v_2 between the particles (X) and their corresponding anti-particles ($\overline{\mathrm{X}}$) as a function of the beam energy. In [12] it was decided to put π^+ and K^+ to the particle group and π^- and K^- to the anti-particle group. The elliptic flow for the particle group is always larger than for the anti-particle group, except for the pions.

Blast-wave fits to v_2 data at energies from $\sqrt{s_{\mathrm{NN}}} = 7.7$ up to 2760 GeV were already done in [66]. They found a larger flow velocity for anti-particles than for particles. The difference decrease with increasing beam energy and approaches zero for 200 and 2760 GeV. The right panel of Fig. 11 depicts the number of protons, anti-protons and net-protons as function of the center-of-mass energy which are shown in [66]. The net-protons correspond to the stopped protons. The anti-proton yield becomes larger with increasing energy while the net-proton number decreases with increasing energy to zero at 2.76 TeV. At 200 GeV the net-proton number is reduced by a factor of four compared to the lower energies. It is obvious that the number of anti-particles is much lower than the number of particles at lower energies. This means the anti-particles represent only a small fraction of the total particles in the event. In addition a better description by the blast-wave model for anti-particles than for particles was observed in [66].

In [57] blast-wave fits to elliptic flow data were done for different centralities, where a larger flow velocity for central collisions than for peripheral collisions was found.

Because of the missing particle and anti-particle spectra at the time of the analysis the underlying effect which leads to the observed differences for particles and anti-particles could not be fully determined. Now the spectra are available and can be included to the fits. For the first time a simultaneous blast-wave fit to the spectra and the elliptic flow data at the BES energies is possible. In contrast to [57, 66] it is not necessary to fix the temperature because it can be now extracted from the fits. This enables an analysis of the dependence between the freeze-out temperature and the energy, as well as

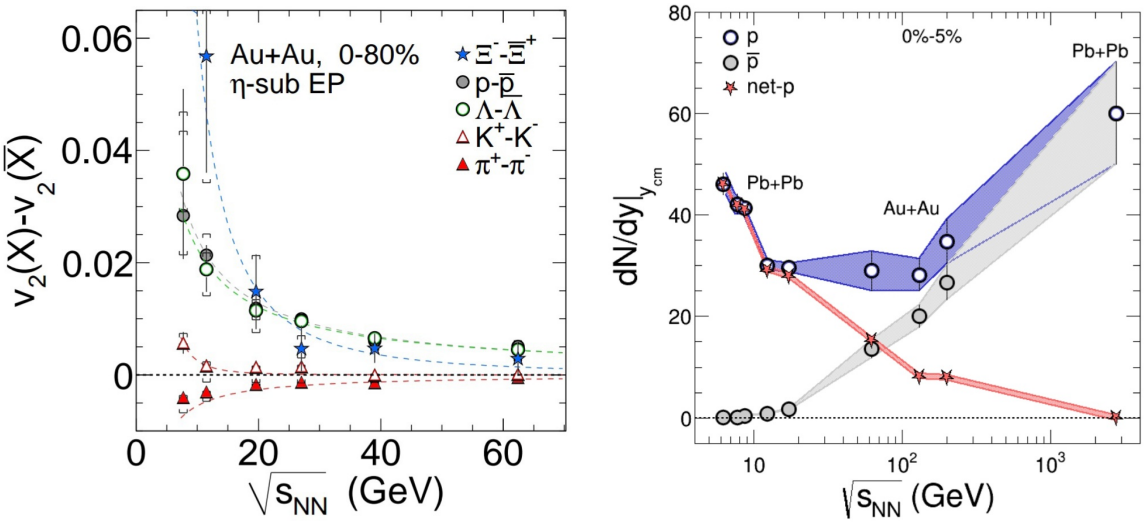

Figure 11: Left: Differences between the v_2-values for particles X and anti-particles $\overline{\mathrm{X}}$ in dependence of $\sqrt{s_{\mathrm{NN}}}$ shown in [12]. Right: Number of protons, anti-protons and net-protons as function of the center-of-mass energy shown in [66].

the freeze-out temperature and the flow velocity.

Because of the reasons described above particles and anti-particles are fitted separately, accordingly we do not expect the same freeze-out temperature and flow velocity for both fits. The fits to particles always include K^+, p and Λ, while the fits to anti-particles include K^-, $\overline{\mathrm{p}}$ and $\overline{\Lambda}$. The used data is listed in Tab. 5. The v_2 data for the particles and anti-particles is available at 10-40% and the spectra are available at 30-40% or 20-40%. In addition there are some small deviations between the spectra at $\sqrt{s_{\mathrm{NN}}} = 62.4$ GeV compared to the spectra at the other energies.

In the next sections exemplarily the simultaneous fits to spectra and elliptic flow data at $\sqrt{s_{\mathrm{NN}}} = 39$ and 11.5 GeV are shown. An analysis of the dependence between the freeze-out temperature, the flow velocity and the beam energy follows. The fit results obtained in the previous sections for $\sqrt{s_{\mathrm{NN}}} = 200$ GeV and 2.76, 5.02 TeV are included. Systematic variations as done for $\sqrt{s_{\mathrm{NN}}} = 200$ GeV were not possible within the scope of this thesis. The errors of the fit parameters are thus only statistical ones of a single fit.

4.1 Fit results for $\sqrt{s_{\mathrm{NN}}} = 11.5$ and 39 GeV

In this section the fit results of the simultaneous blast-wave fits to spectra and elliptic flow data measured in Au-Au collisions at $\sqrt{s_{\mathrm{NN}}} = 11.5$ and 39 GeV are presented. As already mentioned the particles (K^+, p and Λ) and the anti-particles (K^-, $\overline{\mathrm{p}}$ and $\overline{\Lambda}$) are fitted separately. For both, particles and anti-particles, a centrality of 10-40% was used for the v_2 data and 30-40% for the spectra. The fit ranges are calculated with equation 10 and $\beta^{\mathrm{max}} = 0.68$.

The results of the fits for $\sqrt{s_{\mathrm{NN}}} = 39$ GeV are shown in Fig. 12. The spectra of the particles (black) and the anti-particles (red) are normalized to their integrals. The fit results are represented by solid lines and the dashed lines depict the fit predictions, which are calculated with the fit parameters from the fit to other particles. Only the particle mass is left as a free parameter.

The spectra of the particles and anti-particles are both in a good agreement with the fit. With exception of the pions, the predicted particle spectra (Ξ^-, Ω^- and d) are slightly better described than the corresponding anti-particle spectra. The predicted anti-particle curves are lower than the data while the curves for the particles agree with the data. For the particles only the Ω^- spectrum deviates more than one sigma from the fit prediction at lower p_{T}. The centrality for Ω^- and $\overline{\Omega}^+$ is different compared to the other particles and anti-particles, which could be the reason for some deviations. The π^- spectrum is in a better agreement with the prediction at lower p_{T} than the π^+ spectrum. The

spectrum of ϕ is slightly better described by the prediction from the fit to the anti-particles (red). The predictions for J/ψ and K^0_s describe the data better, if they are calculated with the results of the fit to the particle group (black). In contrast to the higher energies, the J/ψ spectrum is well described by the blast-wave prediction calculated with the results from the fit to the particles.

The results for the v_2 data are again depicted as solid lines while the dashed lines are the fit predictions. Similar to the spectra, the elliptic flow data for the particles and anti-particles are well described by the fit curves. For $\overline{\Xi}^+$, $\overline{\Omega}^+$ and $\overline{\mathrm{d}}$ a better description is obtained than for the corresponding particles. For the deuteron the deviations between the data and the predicted curve are large. Because of the different centrality ranges used for the deuteron, anti-deuteron, tritium and He_3 (0-80%), compared to the centrality for other particles and anti-particles (10-40%), deviations are expected. The ϕ is clearly better described by the prediction calculated with the results of the fit to the anti-particles (red), while for K^0_s the predictions are almost equal.

The same effect, with a better description of the v_2 data for anti-particles than for particles, was already observed in [66] for the fitted v_2 data. The larger elliptic flow for particles might be a result of the baryon stopping effect, where quarks from the colliding nucleons, transported from $y = y_{\mathrm{beam}}$ to $y = 0$ receive a higher elliptic flow [19]. This effect is missing for anti-quarks because they are only produced due to $\mathrm{q\overline{q}}$ pair production. The description of the spectra and elliptic flow data of the ϕ meson is more precisely with the prediction for the fit to the anti-particles (K^-, $\overline{\mathrm{p}}$ and $\overline{\Lambda}$). In [66] this fact is explained by baryon stopping too, because the strange quarks and anti-quarks of the ϕ mesons are produced quarks and anti-quarks. It is assumed that particles with up and down quarks are most affected by the baryon stopping. The spectra of the particles and anti-particles are both in good agreement with the predictions and the fit results. No significant differences between the two particle groups can be observed at 39 GeV in contrast to 11.5 GeV, where significant but small differences in the shape of K^+, K^- and p, $\overline{\mathrm{p}}$ are observed as shown in Fig. 13. This might be the case because the spectra might not be as sensitive to the baryon stopping as the v_2.

The mean flow velocity can be obtained with equation 7 . It is $\langle\beta\rangle = 0.41 \pm 0.002$ for the particles and $\langle\beta\rangle = 0.468 \pm 0.002$ for the anti-particles. A larger flow velocity for anti-particles compared to their corresponding particles was already observed in [57, 66].

For the fit to the data measured in Au-Au collisions at 11.5 GeV the same particles, centralities and fit ranges are used as described above. Fig. 13 depicts the results of the simultaneous blast-wave fit to the particle and anti-particle spectra and v_2 data. The fit curves are depicted as solid lines, the predictions as dashed lines. The spectra of the particles are slightly better described by the fit than the anti-particles. The χ^2/point value for Λ is four times smaller than for $\overline{\Lambda}$ and for the proton it is about 50 times smaller than for the anti-proton. For the fit predictions it can not be clearly determined if the particles or anti-particles are better described. The spectra of Ω^- and $\overline{\Omega}^+$ are measured at 0-40%, while the prediction is for 30-40% which might lead to some deviations. The prediction for K^0_s calculated with the results of the fit to the particle group (black) is in a better agreement with the data. The ϕ is described well by both curves. In general we observe that the particle and anti-particle spectra are not equal for $\sqrt{s_{\mathrm{NN}}} = 11.5$ GeV.

The v_2 data of K^+, K^-, Λ and $\overline{\Lambda}$ are well described by the fit curves, while the proton is clearly better described than the anti-proton. The predictions for particles and anti-particles describe the data too. Deviations are only observed for the pions and the deuterons, but the centrality range for the deuteron is again different compared to the others. With exception of the pions and the kaons at high p_{T}, the elliptic flow of all particles is larger than the elliptic flow of the corresponding anti-particles. This might be a result of the baryon stopping as already discussed above. The stopped up and down quarks from the incoming nucleons get a higher elliptic flow while they are transported to mid rapidity [19]. This additional v_2 is missing for the produced quarks and anti-quarks. Because anti-baryons consist of produced anti-quarks, they always get a lower elliptic flow. Because the π^+ and π^- consist of both a quark (u/d) and anti-quark ($\overline{\mathrm{u}}/\overline{\mathrm{d}}$), the probability that one of the quarks is

a stopped quark is equal for π^+ and π^-. In contrast to the observations in [66] the anti-particles are in general not better described than the particles. The fit curve of p and Λ is closer to the data points than the corresponding curves for $\overline{\mathrm{p}}$ and $\overline{\Lambda}$. This is in contradiction to the above described effect by baryon stopping, which implies a better description of the anti-baryons because they consist of only produced anti-quarks. K^+, $\mathrm{K}^-$are both in a good agreement with the data. For the predicted curves for particles and anti-particles, no significant differences are observed. For Ω^-, $\overline{\Omega}^+$, Ξ^- and $\overline{\Xi}^+$ the fit predictions are larger than the data. The opposite is observed for the charged pions. ϕ and K^0_s are better described by the prediction of the anti-particles which is in agreement with the observations in [66].

The mean flow velocity is again larger for the anti-particles than for the particles. It is $\langle\beta\rangle = 0.359 \pm 0.006$ for the particles and $\langle\beta\rangle = 0.432 \pm 0.008$ for the anti-particles. The difference between the two flow velocities is almost equal for 39 and 11.5 GeV.

In the next section the behavior of the mean flow velocity and the kinetic freeze-out temperature for particles and anti-particles as a function of the beam energy is studied in more detail.

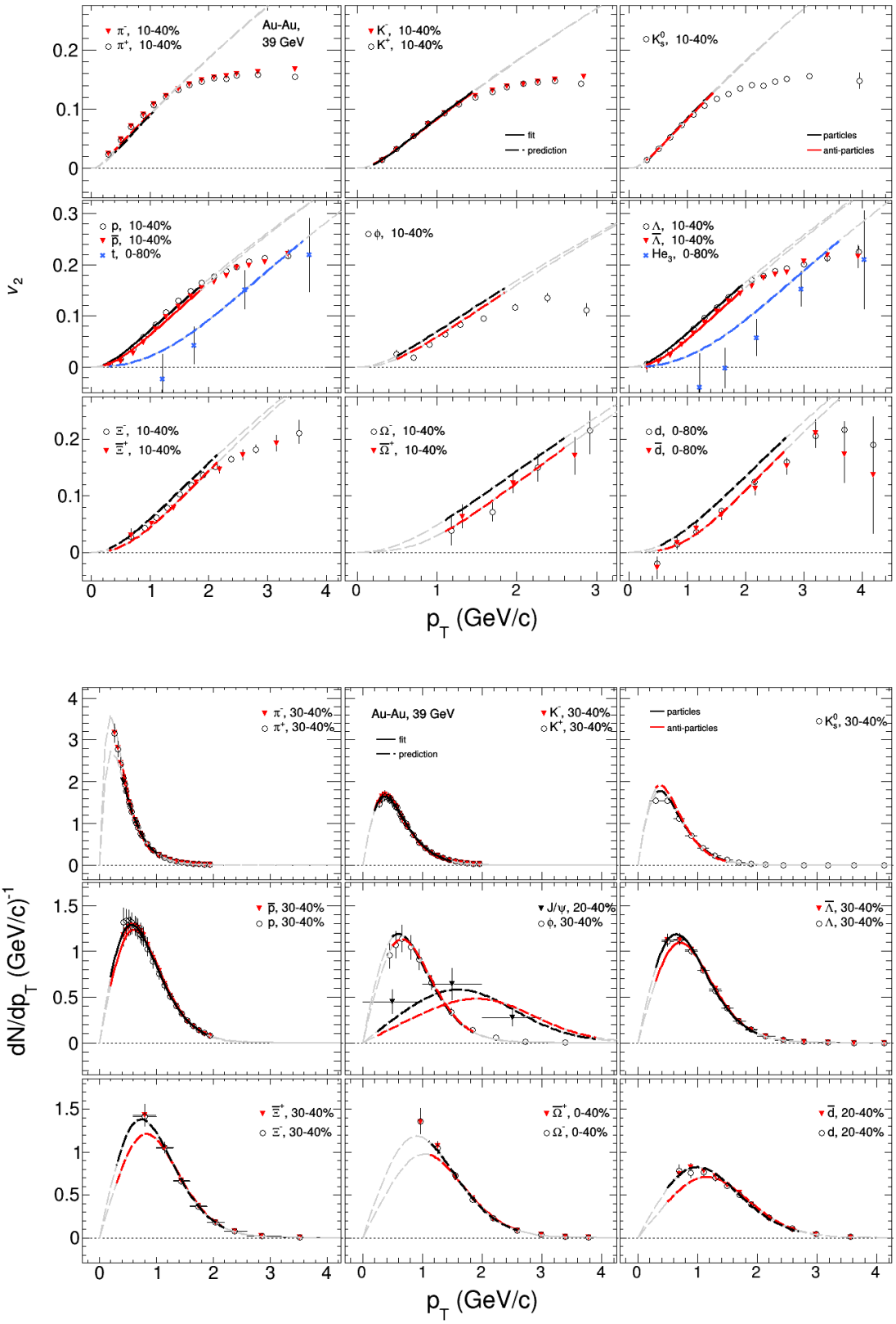

Figure 12: Results of the simultaneous blast-wave fit to spectra and elliptic flow data of K^+, p, Λ and K^-, $\overline{p}$, $\overline{\Lambda}$ at mid-centrality. ϕ, K^0_s and J/ψ are predicted with the results of the fit to the particles (black) and of the fit to the anti-particles (red). Upper: Fit results (solid lines) and predictions (dashed lines) for particle (black) and anti-particle (red) v_2 data. Lower: Fit results (solid lines) and predictions (dashed lines) for particle (black) and anti-particle (red) spectra. The spectra are normalized to their integrals.

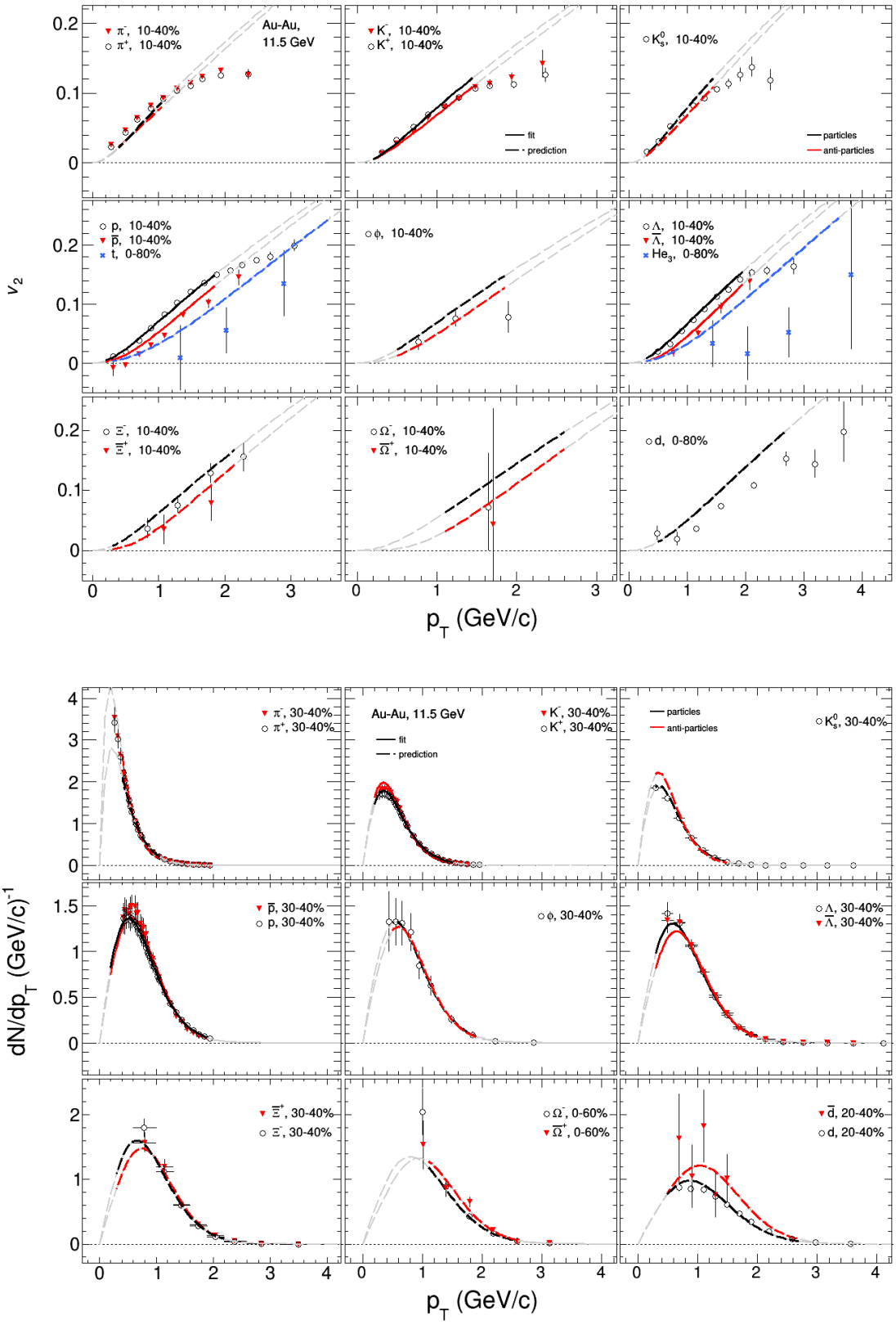

Figure 13: Results of the simultaneous blast-wave fit to spectra and elliptic flow data of K^+, p, Λ and K^-, $\overline{p}$, $\overline{\Lambda}$ at mid-centrality. ϕ and K^0_s are predicted with the results of the fit to the particles (black) and of the fit to the anti-particles (red). Upper: Fit results (solid lines) and predictions (dashed lines) for particle (black) and anti-particle (red) v_2 data. Lower: Fit results (solid lines) and predictions (dashed lines) for particle (black) and anti-particle (red) spectra. The spectra are normalized to their integrals.

4.2 T_{kin} and $\langle\beta\rangle$ in dependence of the center-of-mass energy

The results of the simultaneous blast-wave fits at energies from $\sqrt{s_{\mathrm{NN}}} = 7.7$ GeV up to 5.02 TeV are investigated in this section. First the kinetic freeze-out temperature and the mean flow velocity in dependence of the beam energy are studied, followed by the correlation between T_{kin} and $\langle\beta\rangle$. The data which were used for the fits are listed in Tab. 4 and 5. For the BES energies fits to K^+, p and Λ and K^-, $\overline{\mathrm{p}}$ and $\overline{\Lambda}$ respectively, are done at mid-centrality. The centralities for the spectra are mostly 30-40% and for the v_2 data 10-40%. All fit results for the BES energies are listed in Tab. 8 in the appendix A.3. As already mentioned, particles and anti-particles are fitted separately. The $\phi(\mathrm{s\bar{s}})$ meson is excluded at these lower energies because it is its own anti-particle and can not be clearly assigned to the particle or anti-particle group. Because particle and anti-particle spectra and elliptic flow data are similar at $\sqrt{s_{\mathrm{NN}}} = 200$ GeV, 2.76 and 5.02 TeV, the ϕ is included to the fits at these higher energies. For the data recorded at Au-Au collisions at 200 GeV fits to K, p, ϕ and Λ are done at centralities of 20-40% for the spectra and 0-30% for the v_2 data. The appearing problems due to the different centrality classes were already discussed in section 3.3. Only the K, p and ϕ spectra are available at 2.76 TeV and only the K and p spectra at 5.02 TeV. The centrality for the spectra and v_2 data is 30-40% for all fitted particles at those two energies.

The data and the resulting fits at 14.5 GeV are needed to be considered separately because at the time at which the 14.5 GeV data was recorded the heavy flavour tracker (HFT) was already installed at the STAR experiment [57]. This results in a larger background for the proton spectra due to several nuclear interactions with the additional material between the beam pipe and the TPC, which was not fully corrected. In addition to that the spectra for Λ and $\overline{\Lambda}$ are not available at mid-centrality. Due to these differences the results of the fits to 14.5 GeV data can not be fully compared to the fits at other energies. For completeness they are included in Fig. 14 but not considered in the discussion.

Due to the availability of the spectra of the particles and anti-particles for the BES energies it is now possible to obtain the kinetic freeze-out temperature from the fits. This was not the case for [66]. The upper panel of Fig. 14 depicts the kinetic freeze-out temperature as function of the beam energy. A clear separation between the freeze-out temperatures of the particles and anti-particles can be observed for 7.7-62.4 GeV, where T_{kin} is always larger for the particle than for the anti-particle group. Fluctuations of the temperature around a constant value for energies from 11.5 up to 62.4 GeV are similar to the observations in [61], where fits to π, K and p spectra were presented. In general the temperature is about 10 MeV larger than in [61], but within their experimental uncertainties. The kinetic freeze-out temperature for the anti-particles increases with increasing beam energy between 14.5-62.4 GeV in contrary to the behavior of the particles. The obtained temperatures from the fits to anti-particle data measured at 7.7 and 11.5 GeV do not fully follow this trend. In addition the error bars are significantly larger compared to the higher energies. As already seen in section 4.1, the v_2 data of the anti-proton is not fully described by the fit predictions at 11.5 GeV.

The two curves of the particle and anti-particle group get together at 200 GeV. The obtained kinetic freeze-out temperature of $T_{\mathrm{kin}} = 128.6 \pm 0.6$ MeV is about 20 MeV larger than in [58], where fits to π, K and p spectra at 200 GeV are done. As already seen in section 3.3 a lower temperature is achieved if the pions were included to the fits. The freeze-out temperature for 2.76 TeV is slightly lower than for 200 GeV and decreases of about 15 MeV for 5.02 TeV. The same effect with almost constant kinetic freeze-out temperature for the BES energies and decreasing temperature at LHC energies was already observed in [61]. They explained this observation by more hadronic interaction due to the higher beam energy which results in a later kinetic freeze-out of the particles.

The lower panel of Fig. 14 depicts the mean flow velocity $\langle\beta\rangle$, which is calculated using equation 7 with $n = 1$, in dependence of the beam energy. As for the freeze-out temperature a clear separation between the particles and anti-particles at the BES energies is observed. The flow velocity for the particles is always smaller than for the anti-particles while the freeze-out temperature for the particle is

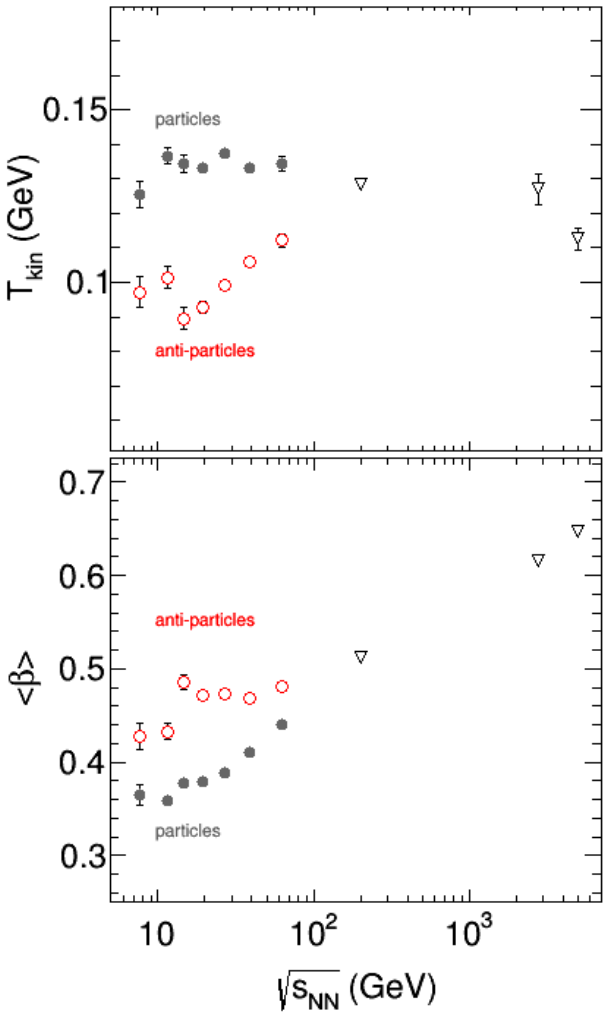

Figure 14: T_{kin} (upper) and $\langle\beta\rangle$ (lower) as function of the center-of-mass energy.

always larger than for the anti-particle group. This anti-correlation between the freeze-out temperature and the flow velocity was already observed in [24, 61].

Basically the same trend as in [66], where fits to particle and anti-particle v_2 data are presented, can be observed here. The flow velocity for the particles increase almost monotonically with increasing beam energy, despite the jump at 7.7 and 11.5 GeV. The flow velocities of the anti-particles fluctuate around a constant value for energies from 19.6 GeV up to 62.4 GeV, where a small increase is observed to 200 GeV. The values for 7.7 and 11.5 GeV are lower than in [66]. An explanation why the differences between particles and anti-particles are not more distinct at lower energies might be the included particle spectra. It is possible that the spectra dominate the fit due to their larger number of data points.

At energies larger than 62.4 GeV a clear increase of the flow velocity for both particles and anti-particles is observed. A reason for that might be a larger initial pressure and energy density at higher beam energies which results in a faster expansion. In [67] an increase in the flow velocity of 10% from 200 GeV to 2.76 TeV is observed, while here the mean flow velocity is about 20% higher for 2.76 TeV. The value of the flow velocity is almost equal for 2.76 TeV to that obtained in [67] from fits to the π, K and p spectra, however the kinetic freeze-out temperature is about 15 MeV higher for our fits to the spectra and v_2 data.

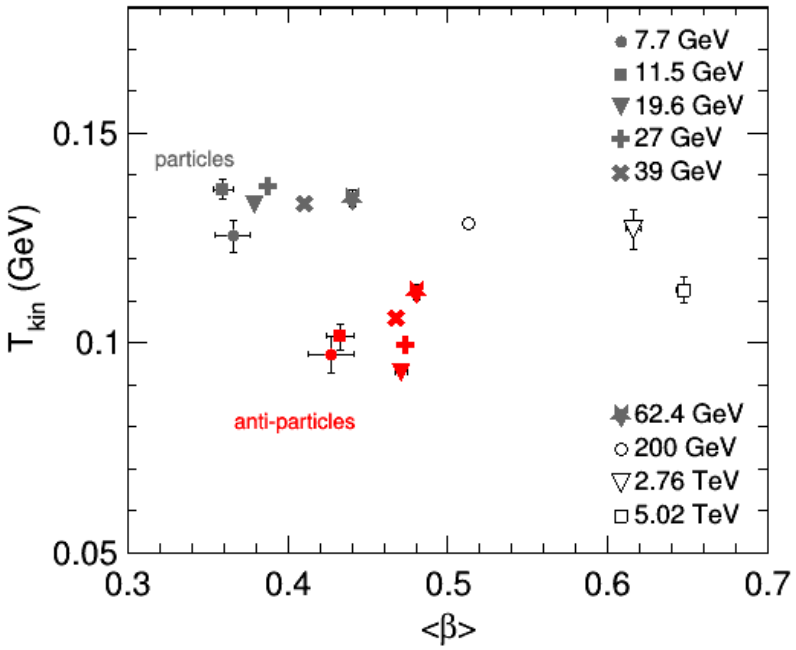

Figure 15: Dependence of the kinetic freeze-out temperature and the mean flow velocity for particles (gray) and anti-particles (red) at $\sqrt{s_{\mathrm{NN}}} = 7.7$ GeV - 5.02 TeV.

Possible explanations for the larger flow velocity for anti-particles than for particles at lower center-of-mass energies are discussed in [66]. It is speculated that anti-protons which are produced in the center of the collision might annihilate while they are flowing to the surface. This leads to the assumption that the measured anti-protons were produced near the surface, where the flow velocity is the largest. Because the $\overline{\mathrm{p}}$/p ratio gets closer to one for higher beam energies, less $\overline{\mathrm{p}}$ annihilate and their contribution from the center becomes larger. This eventually leads to a decrease in the difference of the flow velocity for particles and anti-particles. In [68] a hybrid model, which combines effects such as baryon stopping and the particle transport with the hydrodynamic expansion of the QGP, is presented.

Fig. 15 depicts the summary of the fit results with the mean flow velocity on the x-axis and the kinetic freeze-out temperature on the y-axis. The results of the fit to the 14.5 GeV data are not shown because of the differences in the measurement as described above. As already seen in Fig. 14, $\langle\beta\rangle$ and T_{kin} are clearly separated for the particles and anti-particles at the BES energies. The results of the fits to the particles are in an area of higher T_{kin} and lower $\langle\beta\rangle$, while the fit results of the fits to the anti-particles are at higher $\langle\beta\rangle$ and lower T_{kin}. For the particle group T_{kin} and $\langle\beta\rangle$ are almost anti-correlated. The mean flow velocity is clearly increasing with increasing beam energy, while the kinetic freeze-out temperature slightly decreases. The anti-particle group behaves very differently. A drop of the kinetic freeze-out temperature is observed between 200 and 62.4 GeV and then the temperature is decreasing while the mean flow velocity is almost constant until 19.6 GeV. The results for 7.7 and 11.5 GeV are separated which leads to a non monotonic behavior of the arrangement of the points for the anti-particles. A minimum or maximum is expected between 11.5 and 19.6 GeV. There are speculations from the STAR collaboration, which are based on measurements of the net-proton

distribution, about the existence of the critical point between these energies [69, 70]. Fluctuations around an energy of 14.5 GeV were observed which were interpreted as the increasing fluctuations during a phase transition. If this is true, changes in $\langle\beta\rangle$ and T_{kin} are expected at this energy. Because of systematic uncertainties for the fits at 7.7 and 11.5 GeV to the anti-particles further investigations, which could not be done in the scope of this thesis, are necessary. Fits at other centralities with additional systematic variations of the fit ranges and start parameters should be done.

In [71] the fluctuations are explained as a result of the baryon number conservation. The differences between particles and anti-particles possibly arise from the effect of baryon stopping. As already seen in Fig. 11 those differences decrease for increasing beam energy, since the number of stopped particles decreases at higher energies. A clear increase of the net-baryon number as function of the rapidity for lower energies is displayed in [71] too. Therefore fits to the particles at lower energies are influenced by the stopped particles and thus the results for anti-particles are more reliable.

At least a fully thermalized system can not be expected due to the differences between particles and anti-particles at lower energies.

5 Summary and Outlook

In this bachelor thesis simultaneous blast-wave fits to spectra and elliptic flow data at various beam energies were presented. The blast-wave model which is provided in [24] was used. The first part of this thesis was dedicated to the importing of new data to the main program which is used for the blast-wave fits. Data at energies from $\sqrt{s_{\mathrm{NN}}} = 7.7$ GeV up to 5.02 TeV were converted into a unified format which could then be used in the main program. There are some modifications done for the importing method of new data. It is now possible to add new data easily without changing something in the program. The selection of the data for the fits is now possible with the GUI.

Blast-wave fits to spectra and elliptic flow data measured in high energy collisions at $\sqrt{s_{\mathrm{NN}}} =$ 200 GeV, 2.76 and 5.02 TeV are done for further investigations of the question if heavy quarks are thermalized in the QGP. Fits, which were already done in [24], are reproduced for the verification of the program. Except for some minor deviations the same results were obtained. In addition a fit to 5.02 TeV were included, where a reasonable agreement with the data was found. In particular the Υ elliptic flow is very well described by the blast-wave prediction which might be an indication for a possible thermalization of the bottom quarks.

In the next section systematic studies of the fits to 200 GeV were presented. Various collision centralities, systematic variations of the fit ranges and different sets of particles, which were included to the fits, were studied. A good agreement with the data was observed. Similar to the bottom quarks for higher LHC energies the charm quark and thus the D^0 and J/ψ mesons were of particular interest. Their elliptic flow data could also be described by the blast-wave model but for the spectra larger deviations were observed. Different factors might influence the results. Due to the different centrality ranges for v_2 and dN/dp_{T} some deviations were expected. For the v_2 data only 0-30% or 30-80% were available, while for the most spectra 20-40% could be used. More precise results are expected if the same centrality ranges are used in the fits. In addition it is possible that other physics needs to be included to find a better description of the J/ψ spectra, because we observed significant differences in the shapes of the data and the fit. For further investigations fits with the calculated feed-down contributions can be studied [26].

In the second part of the analysis simultaneous blast-wave fits to spectra and elliptic flow data to the BES energies were carried out, where the spectra could be included to the fits for the first time. This enables the investigation of the kinetic freeze-out temperature. Since the particle and anti-particle elliptic flow data are not equal at this lower energies, they were fitted separately. Standard fits to K^+, p, Λ and K^-, $\overline{\mathrm{p}}$, $\overline{\Lambda}$ were carried out at mid-centrality. The fit results for $\sqrt{s_{\mathrm{NN}}} = 11.5$ and 39 GeV were shown in detail. A good agreement of the blast-wave model for the particles and anti-particles were found, except some small differences between the data and the fit results for the $\overline{\mathrm{p}}$ at 11.5 GeV.

The extracted kinetic freeze-out temperatures and flow velocities were studied as a function of the beam-energy. For that the previous fit results for 200 GeV and 2.76, 5.02 TeV were included. A clear separation between the particles and anti-particles at lower energies was observed. While a higher temperature was obtained for the particles, the flow velocity is in general larger for the anti-particles. The splitting between particles and anti-particles becomes smaller for higher energies until they reach equal values at $\sqrt{s_{\mathrm{NN}}} \geq 200$ GeV. Deviations from this monotonic behavior were observed for the lowest energies, 7.7 and 11.5 GeV. Additional studies at those two energies are necessary, which can be done with the data measured in the BES phase II [72]. An explanation for the splitting between particles and anti-particles is given by the baryon stopping. The particles could be influenced by the stopped quarks from the incoming nuclei.

For further investigations fits to data measured at more central or peripheral collisions should be done. The resulting pattern for the temperature and flow velocity should be compared to the results at mid-centrality shown in this bachelor thesis. As part of this bachelor thesis a fit to the HADES

data measured at $\sqrt{s_{\mathrm{NN}}} = 2.4$ GeV were carried out. The fit results should be included as soon as the data is published.

A Appendix

A.1 Boost model

Formulas of the transverse momentum spectra and elliptic flow for the boost model [25].

$$\frac{1}{2\pi p_{\mathrm{T}}}\frac{\mathrm{d}N}{\mathrm{d}p_{\mathrm{T}}\mathrm{d}y} \propto \int_0^1 \hat{r}\mathrm{d}\hat{r}\int_0^{2\pi}\mathrm{d}\hat{\phi}\; T[\xi_{\mathrm{m}}I_0(\xi_{\mathrm{p}})K_1(\xi_{\mathrm{m}}) - \xi_{\mathrm{p}}I_1(\xi_{\mathrm{p}})K_0(\xi_{\mathrm{m}})] \tag{13}$$

$$v_2(p_{\mathrm{T}}) = \frac{n_{v_2}(p_{\mathrm{T}})}{d_{v_2}(p_{\mathrm{T}})} \tag{14}$$

$$n_{v_2}(p_{\mathrm{T}}) = \int_0^1 \hat{r}\mathrm{d}\hat{r}\int_0^{2\pi}\mathrm{d}\hat{\phi}\;\cos 2\phi_b[2I_2(\xi_{\mathrm{p}})K_0(\xi_{\mathrm{m}}) + \xi_{\mathrm{m}}I_2(\xi_{\mathrm{p}})K_1(\xi_{\mathrm{m}}) - \xi_{\mathrm{p}}I_1(\xi_{\mathrm{p}})K_0(\xi_{\mathrm{m}})] \tag{15}$$

$$d_{v_2}(p_{\mathrm{T}}) = \int_0^1 \hat{r}\mathrm{d}\hat{r}\int_0^{2\pi}\mathrm{d}\hat{\phi}\;[\xi_{\mathrm{m}}I_0(\xi_{\mathrm{p}})K_1(\xi_{\mathrm{m}}) - \xi_{\mathrm{p}}I_1(\xi_{\mathrm{p}})K_0(\xi_{\mathrm{m}})] \tag{16}$$

A.2 Fit results for $\sqrt{s_{\mathrm{NN}}} = 200$ GeV

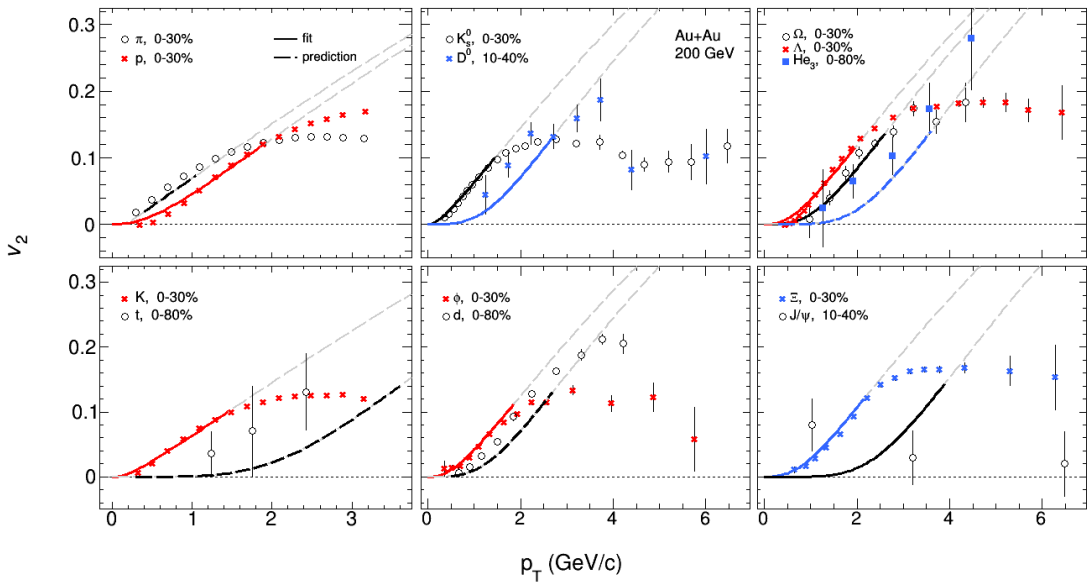

Figure 16: Fit results for the v_2 data, fitted with the boost model at $\sqrt{s_{\mathrm{NN}}} = 200$ GeV. The solid lines are the fit results and the dashed lines the fit predictions. The fitted particles are K, p, ϕ, Ξ, Ω, Λ, $\mathrm{K}^0_{\mathrm{s}}$, D^0, J/ψ with $\beta^{\max} = 0.68$.

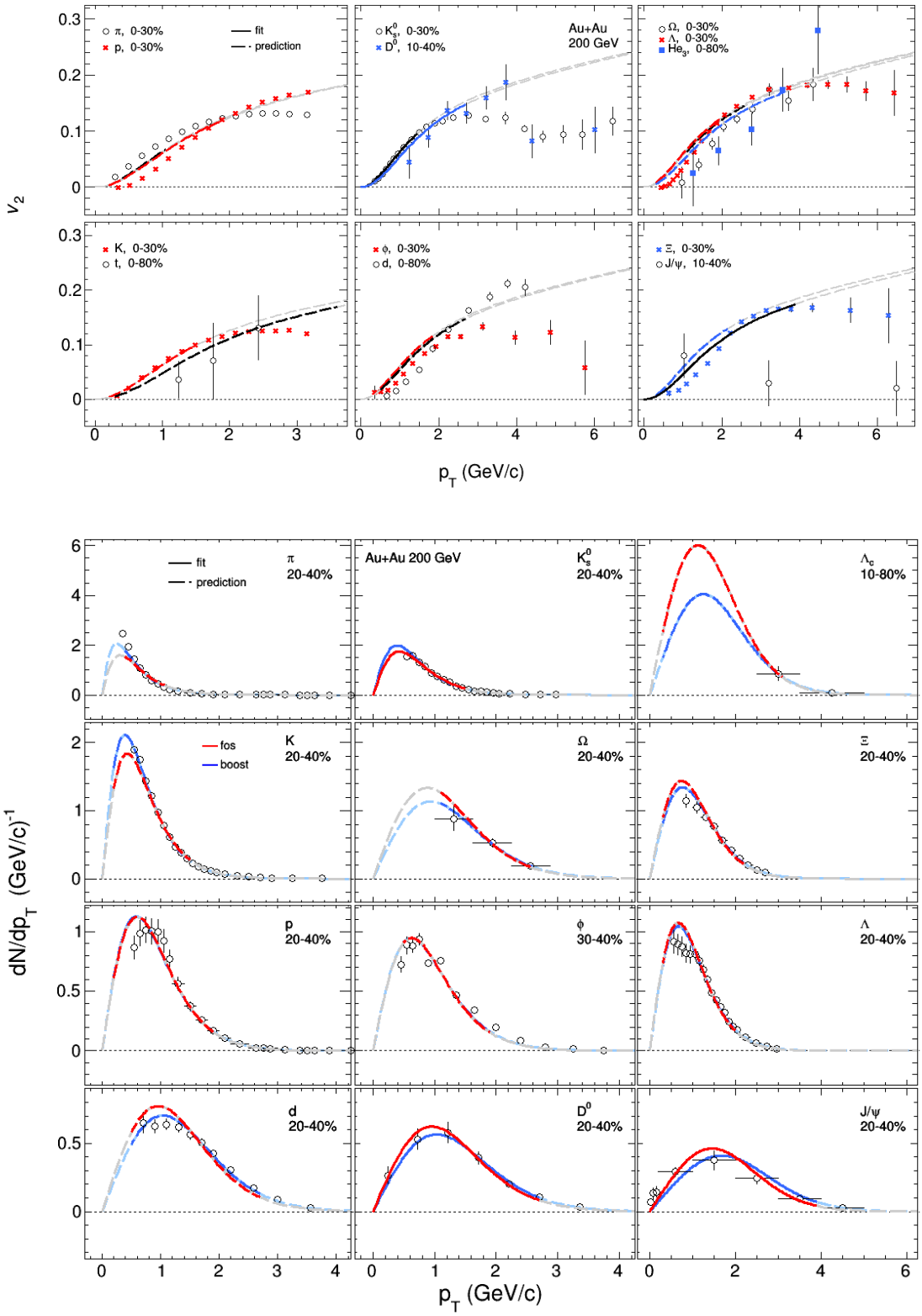

Figure 17: Simultaneous blast-wave fit results (solid lines) and predictions (dashed lines) from a fit to K^0_s, D^0 and J/ψ with $\beta^{max} = 0.68$. Upper: Results for the v_2 data with the standard blast-wave model. Lower: Results (red) and predictions (gray) for the spectra, obtained with the standard blast-wave model ("fos") and the boost model ("boost"), where results and predictions are shown in blue. The spectra are normalized to their integrals.

A.3 Fit parameters for $\sqrt{s_{\rm NN}}$ = 7.7 - 62.4 GeV

Table 8: Blast-wave fit results for $\sqrt{s_{\rm NN}}$ = 7.7 - 62.4 GeV at mid-centrality. For the particle group (X) the results are from fits to K^+, p and Λ and for the anti-particle group ($\overline{\rm X}$) K^-, $\overline{\rm p}$ and $\overline{\Lambda}$ are fitted. At $\sqrt{s_{\rm NN}}$ = 14.5 GeV the Λ and $\overline{\Lambda}$ spectra are missing. The fit ranges are based on Eqn. 10 with $\beta^{\rm max} = 0.68$.

$\sqrt{s_{\rm NN}}$ (GeV)		$T_{\rm kin}$ (MeV)	ρ_0	ρ_2	R_x/R_y
7.7	X	125.5 ± 3.8	0.57 ± 0.02	0.033 ± 0.002	0.845 ± 0.011
	$\overline{\rm X}$	97.1 ± 4.4	0.68 ± 0.03	0.024 ± 0.005	0.928 ± 0.017
11.5	X	136.7 ± 2.3	0.56 ± 0.01	0.040 ± 0.001	0.818 ± 0.008
	$\overline{\rm X}$	101.4 ± 3.2	0.69 ± 0.02	0.037 ± 0.002	0.924 ± 0.006
14.5	X	134.5 ± 2.6	0.59 ± 0.01	0.043 ± 0.001	0.831 ± 0.007
	$\overline{\rm X}$	89.6 ± 3.1	0.79 ± 0.02	0.033 ± 0.001	0.914 ± 0.003
19.6	X	133.0 ± 1.4	0.60 ± 0.01	0.044 ± 0.001	0.832 ± 0.004
	$\overline{\rm X}$	92.8 ± 1.7	0.77 ± 0.01	0.035 ± 0.001	0.911 ± 0.002
27.0	X	137.3 ± 1.3	0.61 ± 0.004	0.047 ± 0.001	0.829 ± 0.003
	$\overline{\rm X}$	99.3 ± 1.2	0.77 ± 0.003	0.039 ± 0.001	0.902 ± 0.001
39.0	X	133.2 ± 1.1	0.65 ± 0.003	0.048 ± 0.0005	0.841 ± 0.002
	$\overline{\rm X}$	105.9 ± 1.2	0.76 ± 0.004	0.044 ± 0.0005	0.892 ± 0.001
62.4	X	134.5 ± 2.0	0.70 ± 0.004	0.055 ± 0.001	0.851 ± 0.003
	$\overline{\rm X}$	112.2 ± 1.8	0.78 ± 0.004	0.050 ± 0.001	0.886 ± 0.002

Bibliography

[1] *CERN Webpage*, https://home.cern/science/physics/heavy-ions-and-quark-gluon-plasma, 2020. (visited on 07/13/2020).

[2] U. W. Heinz, "The Strongly coupled quark-gluon plasma created at RHIC", *J. Phys. A*, vol. 42, D. Neilson and G. Senatore, Eds., p. 214 003, 2009. arXiv: 0810.5529 [nucl-th].

[3] J. Adams *et al.*, "Experimental and theoretical challenges in the search for the quark gluon plasma: The STAR Collaboration's critical assessment of the evidence from RHIC collisions", *Nucl. Phys. A*, vol. 757, pp. 102–183, 2005. arXiv: nucl-ex/0501009.

[4] K. Adcox *et al.*, "Formation of dense partonic matter in relativistic nucleus-nucleus collisions at RHIC: Experimental evaluation by the PHENIX collaboration", *Nucl. Phys. A*, vol. 757, pp. 184–283, 2005. arXiv: nucl-ex/0410003.

[5] M. Aggarwal *et al.*, "An Experimental Exploration of the QCD Phase Diagram: The Search for the Critical Point and the Onset of De-confinement", Jul. 2010. arXiv: 1007.2613 [nucl-ex].

[6] L. Adamczyk *et al.*, "Measurements of jet quenching with semi-inclusive hadron+jet distributions in Au+Au collisions at $\sqrt{s_{NN}} = 200$ GeV", *Phys. Rev. C*, vol. 96, no. 2, p. 024 905, 2017. arXiv: 1702.01108 [nucl-ex].

[7] C. Gale, S. Jeon, and B. Schenke, "Hydrodynamic Modeling of Heavy-Ion Collisions", *Int. J. Mod. Phys.*, vol. A28, p. 1 340 011, 2013. arXiv: 1301.5893 [nucl-th].

[8] M. Thomson, *Modern Particle Physics* -. Cambridge: Cambridge University Press, 2013, ISBN: 978-1-107-03426-6.

[9] *CERN Webpage*, https://home.cern/science/physics/higgs-boson, 2020. (visited on 05/15/2020).

[10] M. T. et al. (Particle Data Group), *Phys. Rev. D 98, 030001*, (2018) and 2019 update.

[11] P. Z. et al. (Particle Data Group), *Prog. Theor. Exp. Phys. 2020, 083C01*, 2020.

[12] L. Adamczyk *et al.*, "Elliptic flow of identified hadrons in Au+Au collisions at $\sqrt{s_{NN}} = 7.7$-62.4 GeV", *Phys. Rev. C*, vol. 88, p. 014 902, 2013. arXiv: 1301.2348 [nucl-ex].

[13] K. Reygers and J. Stachel, *Quark-Gluon Plasma Physics Lecture*, https://www.physi.uni-heidelberg.de/~reygers/lectures/2019/qgp/qgp_lecture_ss2019.html, 2019. (visited on 05/22/2020).

[14] *GSI Webpage*, https://www.gsi.de/en/researchaccelerators/fair.htm, 2020. (visited on 05/15/2020).

[15] U. W. Heinz, "Early collective expansion: Relativistic hydrodynamics and the transport properties of QCD matter", *Landolt-Bornstein*, vol. 23, p. 240, 2010. arXiv: 0901.4355 [nucl-th].

[16] R. Stock, "Relativistic Nucleus-Nucleus Collisions and the QCD Matter Phase Diagram", Jul. 2008. arXiv: 0807.1610 [nucl-ex].

[17] C. Adler *et al.*, "Identified particle elliptic flow in Au + Au collisions at $\sqrt{s_{\mathrm{NN}}} = 130$-GeV", *Phys. Rev. Lett.*, vol. 87, p. 182 301, 2001. arXiv: nucl-ex/0107003 [nucl-ex].

[18] P. Huovinen, P. F. Kolb, U. W. Heinz, P. V. Ruuskanen, and S. A. Voloshin, "Radial and elliptic flow at RHIC: Further predictions", *Phys. Lett.*, vol. B503, pp. 58–64, 2001. arXiv: hep-ph/0101136 [hep-ph].

[19] J. Dunlop, M. Lisa, and P. Sorensen, "Constituent quark scaling violation due to baryon number transport", *Phys. Rev. C*, vol. 84, p. 044 914, 2011. arXiv: 1107.3078 [hep-ph].

[20] H. Masui, *Elliptic flow*, http://rnc.lbl.gov/Poskanzer/BonnerTalk/BonnerTalk.pdf, 2008. (visited on 06/27/2020).

[21] M. L. Miller, K. Reygers, S. J. Sanders, and P. Steinberg, "Glauber modeling in high energy nuclear collisions", *Ann. Rev. Nucl. Part. Sci.*, vol. 57, pp. 205–243, 2007. arXiv: nucl-ex/0701025.

[22] E. Schnedermann, J. Sollfrank, and U. W. Heinz, "Thermal phenomenology of hadrons from 200-A/GeV S+S collisions", *Phys. Rev.*, vol. C48, pp. 2462–2475, 1993. arXiv: nucl-th/9307020 [nucl-th].

[23] F. Retiere and M. A. Lisa, "Observable implications of geometrical and dynamical aspects of freeze out in heavy ion collisions", *Phys. Rev.*, vol. C70, p. 044 907, 2004. arXiv: nucl-th/0312024 [nucl-th].

[24] K. Reygers, A. Schmah, A. Berdnikova, and X. Sun, "Blast-wave description of Upsilon elliptic flow at LHC energies", *Phys. Rev. C*, vol. 101, no. 6, p. 064 905, 2020. arXiv: 1910.14618 [hep-ph].

[25] A. Berdnikova, N. Grünwald, K. Reygers, A. Schmah, N. Schmal, and X. Sun, publication in preparation.

[26] N. Schmal, *Blast-wave fits with feed-down*, bachelor thesis, private communication, 2020.

[27] *CERN ROOT Webpage*, https://root.cern/about/, 2020. (visited on 07/13/2020).

[28] *HEPData Webpage*, https://www.hepdata.net/, 2020. (visited on 07/14/2020).

[29] *PDG Webpage*, http://pdg.lbl.gov/2020/listings/contents_listings.html, 2020. (visited on 06/22/2020).

[30] S. Acharya *et al.*, "Anisotropic flow of identified particles in Pb-Pb collisions at $\sqrt{s_{\mathrm{NN}}} = 5.02$ TeV", *JHEP*, vol. 09, p. 006, 2018. arXiv: 1805.04390 [nucl-ex].

[31] S. Acharya *et al.*, "Production of charged pions, kaons and (anti-)protons in Pb-Pb and inelastic pp collisions at $\sqrt{s_{\mathrm{NN}}} = 5.02$ TeV", *Phys. Rev. C*, vol. 101, no. 4, p. 044 907, 2020. arXiv: 1910.07678 [nucl-ex].

[32] S. Acharya *et al.*, "J/ψ elliptic and triangular flow in Pb-Pb collisions at $\sqrt{s_{\mathrm{NN}}} = 5.02$ TeV", May 2020. arXiv: 2005.14518 [nucl-ex].

[33] S. Acharya *et al.*, "Centrality and transverse momentum dependence of inclusive J/ψ production at midrapidity in Pb-Pb collisions at $\sqrt{s_{\mathrm{NN}}} = 5.02$ TeV", *Phys. Lett. B*, vol. 805, p. 135 434, 2020. arXiv: 1910.14404 [nucl-ex].

[34] S. Acharya *et al.*, "Measurement of Υ(1S) elliptic flow at forward rapidity in Pb-Pb collisions at $\sqrt{s_{\mathrm{NN}}} = 5.02$ TeV", 2019. arXiv: 1907.03169 [nucl-ex].

[35] B. B. Abelev *et al.*, "Elliptic flow of identified hadrons in Pb-Pb collisions at $\sqrt{s_{\mathrm{NN}}} = 2.76$ TeV", *JHEP*, vol. 06, p. 190, 2015. arXiv: 1405.4632 [nucl-ex].

[36] J. Adam *et al.*, "Centrality dependence of the nuclear modification factor of charged pions, kaons, and protons in Pb-Pb collisions at $\sqrt{s_{\mathrm{NN}}} = 2.76$ TeV", *Phys. Rev.*, vol. C93, no. 3, p. 034 913, 2016. arXiv: 1506.07287 [nucl-ex].

[37] J. Adam *et al.*, "K$^*(892)^0$ and $\phi(1020)$ meson production at high transverse momentum in pp and Pb-Pb collisions at $\sqrt{s_{\mathrm{NN}}} = 2.76$ TeV", *Phys. Rev.*, vol. C95, no. 6, p. 064 606, 2017. arXiv: 1702.00555 [nucl-ex].

[38] B. B. Abelev *et al.*, "Multi-strange baryon production at mid-rapidity in Pb-Pb collisions at $\sqrt{s_{NN}} = 2.76$ TeV", *Phys. Lett.*, vol. B728, pp. 216–227, 2014, [Erratum: Phys. Lett.B734,409(2014)]. arXiv: 1307.5543 [nucl-ex].

[39] B. Abelev *et al.*, "D meson elliptic flow in non-central Pb-Pb collisions at $\sqrt{s_{\mathrm{NN}}} = 2.76$TeV", *Phys. Rev. Lett.*, vol. 111, p. 102 301, 2013. arXiv: 1305.2707 [nucl-ex].

[40] J. Adam *et al.*, "Transverse momentum dependence of D-meson production in Pb-Pb collisions at $\sqrt{s_{\rm NN}} = 2.76$ TeV", *JHEP*, vol. 03, p. 081, 2016. arXiv: 1509.06888 [nucl-ex].

[41] E. Abbas *et al.*, "J/ψ Elliptic Flow in Pb-Pb Collisions at $\sqrt{s_{\rm NN}} = 2.76$ TeV", *Phys. Rev. Lett.*, vol. 111, p. 162 301, 2013. arXiv: 1303.5880 [nucl-ex].

[42] V. Khachatryan *et al.*, "Suppression of $\Upsilon(1S), \Upsilon(2S)$ and $\Upsilon(3S)$ production in PbPb collisions at $\sqrt{s_{\rm NN}} = 2.76$ TeV", *Phys. Lett.*, vol. B770, pp. 357–379, 2017. arXiv: 1611.01510 [nucl-ex].

[43] S. Acharya *et al.*, "Measurement of deuteron spectra and elliptic flow in Pb–Pb collisions at $\sqrt{s_{\rm NN}} = 2.76$ TeV at the LHC", *Eur. Phys. J.*, vol. C77, no. 10, p. 658, 2017. arXiv: 1707.07304 [nucl-ex].

[44] J. Adam *et al.*, "Production of light nuclei and anti-nuclei in pp and Pb-Pb collisions at energies available at the CERN Large Hadron Collider", *Phys. Rev.*, vol. C93, no. 2, p. 024 917, 2016. arXiv: 1506.08951 [nucl-ex].

[45] L. Adamczyk *et al.*, "Centrality and transverse momentum dependence of elliptic flow of multistrange hadrons and ϕ meson in Au+Au collisions at $\sqrt{s_{NN}} = 200$ GeV", *Phys. Rev. Lett.*, vol. 116, no. 6, p. 062 301, 2016. arXiv: 1507.05247 [nucl-ex].

[46] B. Abelev *et al.*, "Energy dependence of pi+-, p and anti-p transverse momentum spectra for Au+Au collisions at s(NN)**(1/2) = 62.4 and 200-GeV", *Phys. Lett. B*, vol. 655, pp. 104–113, 2007. arXiv: nucl-ex/0703040.

[47] A. Adare *et al.*, "Spectra and ratios of identified particles in Au+Au and d+Au collisions at $\sqrt{s_{NN}} = 200$ GeV", *Phys. Rev. C*, vol. 88, no. 2, p. 024 906, 2013. arXiv: 1304.3410 [nucl-ex].

[48] B. Abelev *et al.*, "Measurements of phi meson production in relativistic heavy-ion collisions at RHIC", *Phys. Rev. C*, vol. 79, p. 064 903, 2009. arXiv: 0809.4737 [nucl-ex].

[49] G. Agakishiev *et al.*, "Strangeness Enhancement in Cu+Cu and Au+Au Collisions at $\sqrt{s_{NN}} =$ 200 GeV", *Phys. Rev. Lett.*, vol. 108, p. 072 301, 2012. arXiv: 1107.2955 [nucl-ex].

[50] L. Adamczyk *et al.*, "Measurement of D^0 Azimuthal Anisotropy at Midrapidity in Au+Au Collisions at $\sqrt{s_{NN}}$=200 GeV", *Phys. Rev. Lett.*, vol. 118, no. 21, p. 212 301, 2017. arXiv: 1701.06060 [nucl-ex].

[51] J. Adam *et al.*, "Centrality and transverse momentum dependence of D^0-meson production at mid-rapidity in Au+Au collisions at $\sqrt{s_{\rm NN}} = 200\,\text{GeV}$", *Phys. Rev. C*, vol. 99, no. 3, p. 034 908, 2019. arXiv: 1812.10224 [nucl-ex].

[52] L. Adamczyk *et al.*, "Measurement of J/ψ Azimuthal Anisotropy in Au+Au Collisions at $\sqrt{s_{NN}}$ = 200 GeV", *Phys. Rev. Lett.*, vol. 111, no. 5, p. 052 301, 2013. arXiv: 1212.3304 [nucl-ex].

[53] J. Adam *et al.*, "Observation of excess J/ψ yield at very low transverse momenta in Au+Au collisions at $\sqrt{s_{\rm NN}} = 200$ GeV and U+U collisions at $\sqrt{s_{\rm NN}} = 193$ GeV", *Phys. Rev. Lett.*, vol. 123, no. 13, p. 132 302, 2019. arXiv: 1904.11658 [hep-ex].

[54] L. Adamczyk *et al.*, "Measurement of elliptic flow of light nuclei at $\sqrt{s_{NN}} = 200$, 62.4, 39, 27, 19.6, 11.5, and 7.7 GeV at the BNL Relativistic Heavy Ion Collider", *Phys. Rev. C*, vol. 94, no. 3, p. 034 908, 2016. arXiv: 1601.07052 [nucl-ex].

[55] J. Adam *et al.*, "Beam energy dependence of (anti-)deuteron production in Au + Au collisions at the BNL Relativistic Heavy Ion Collider", *Phys. Rev. C*, vol. 99, no. 6, p. 064 905, 2019. arXiv: 1903.11778 [nucl-ex].

[56] J. Adam *et al.*, "Observation of enhancement of charmed baryon-to-meson ratio in Au+Au collisions at $\sqrt{s_{NN}} = 200$ GeV", *Phys. Rev. Lett.*, vol. 124, no. 17, p. 172 301, 2020. arXiv: 1910.14628 [nucl-ex].

[57] L. Adamczyk *et al.*, "Centrality dependence of identified particle elliptic flow in relativistic heavy ion collisions at $\sqrt{s_{NN}}$=7.7–62.4 GeV", *Phys. Rev.*, vol. C93, no. 1, p. 014 907, 2016. arXiv: 1509.08397 [nucl-ex].

[58] B. I. Abelev *et al.*, "Systematic Measurements of Identified Particle Spectra in pp, d^+ Au and Au+Au Collisions from STAR", *Phys. Rev.*, vol. C79, p. 034 909, 2009. arXiv: 0808.2041 [nucl-ex].

[59] M. Aggarwal *et al.*, "Strange and Multi-strange Particle Production in Au+Au Collisions at $\sqrt{s_{NN}}$ = 62.4 GeV", *Phys. Rev. C*, vol. 83, p. 024 901, 2011. arXiv: 1010.0142 [nucl-ex].

[60] L. Adamczyk *et al.*, "Energy dependence of J/ψ production in Au+Au collisions at $\sqrt{s_{NN}}$ = 39, 62.4 and 200 GeV", *Phys. Lett. B*, vol. 771, pp. 13–20, 2017. arXiv: 1607.07517 [hep-ex].

[61] L. Adamczyk *et al.*, "Bulk Properties of the Medium Produced in Relativistic Heavy-Ion Collisions from the Beam Energy Scan Program", *Phys. Rev. C*, vol. 96, no. 4, p. 044 904, 2017. arXiv: 1701.07065 [nucl-ex].

[62] L. Adamczyk *et al.*, "Probing parton dynamics of QCD matter with Ω and ϕ production", *Phys. Rev. C*, vol. 93, no. 2, p. 021 903, 2016. arXiv: 1506.07605 [nucl-ex].

[63] J. Adam *et al.*, "Strange hadron production in Au+Au collisions at $\sqrt{s_{\rm NN}}$ = 7.7, 11.5, 19.6, 27, and 39 GeV", Jun. 2019. arXiv: 1906.03732 [nucl-ex].

[64] J. Adam *et al.*, "Bulk properties of the system formed in $Au+Au$ collisions at $\sqrt{s_{\rm NN}}$ =14.5 GeV at the BNL STAR detector", *Phys. Rev. C*, vol. 101, no. 2, p. 024 905, 2020. arXiv: 1908.03585 [nucl-ex].

[65] *TMinuit Class Reference*, https://root.cern.ch/doc/master/classTMinuit.html, 2020. (visited on 07/16/2020).

[66] X. Sun, H. Masui, A. M. Poskanzer, and A. Schmah, "Blast Wave Fits to Elliptic Flow Data at $\sqrt{s_{\rm NN}}$ = 7.7–2760 GeV", *Phys. Rev.*, vol. C91, no. 2, p. 024 903, 2015. arXiv: 1410.1947 [hep-ph].

[67] B. Abelev *et al.*, "Centrality dependence of π, K, p production in Pb-Pb collisions at $\sqrt{s_{NN}}$ = 2.76 TeV", *Phys. Rev.*, vol. C88, p. 044 910, 2013. arXiv: 1303.0737 [hep-ex].

[68] J. Steinheimer, V. Koch, and M. Bleicher, "Hydrodynamics at large baryon densities: Understanding proton vs. anti-proton v_2 and other puzzles", *Phys. Rev. C*, vol. 86, p. 044 903, 2012. arXiv: 1207.2791 [nucl-th].

[69] L. Adamczyk *et al.*, "Energy Dependence of Moments of Net-proton Multiplicity Distributions at RHIC", *Phys. Rev. Lett.*, vol. 112, p. 032 302, 2014. arXiv: 1309.5681 [nucl-ex].

[70] J. Adam *et al.*, "Net-proton number fluctuations and the Quantum Chromodynamics critical point", Jan. 2020. arXiv: 2001.02852 [nucl-ex].

[71] P. Braun-Munzinger, B. Friman, K. Redlich, A. Rustamov, and J. Stachel, "Relativistic nuclear collisions: Establishing the non-critical baseline for fluctuation measurements", Jul. 2020. arXiv: 2007.02463 [nucl-th].

[72] *STAR collaboration, "Studying the Phase Diagram of QCD Matter at RHIC"*, Star Note 0598, 2014.

Erklärung

Ich versichere, dass ich diese Arbeit selbstständig verfasst und keine anderen als die angegebenen Quellen und Hilfsmittel benutzt habe.

Heidelberg, den 11.08.2020,

Acknowledgements

First I would like to thank Prof. Dr. Johanna Stachel for giving me the opportunity of being part of the group and getting an insight into this interesting field of research.

I would also like to thank Prof. Dr. Klaus Reygers and Dr. Alexander Schmah for their guidance throughout my thesis, for all the discussions and comments. I appreciate that they let me join their project and made this thesis possible. I wish to give special thanks to Dr. Alexander Schmah, who encouraged me and continuously helped me with problems and questions during the last months. I would like to thank him and Dr. Mesut Arslandok for proofreading my thesis.

Finally, I wish to express my gratitude to my mother and my boyfriend Philipp for their support and patience during the process of writing this thesis and the last years of my study.